

MULTI-YEAR SEARCH FOR A DIFFUSE FLUX OF MUON NEUTRINOS
WITH AMANDA-II

by

JESSICA LOUISE HODGES

A dissertation submitted in partial fulfillment of the
requirements for the degree of

DOCTOR OF PHILOSOPHY
(PHYSICS)

at the

UNIVERSITY OF WISCONSIN – MADISON

2007

© Copyright by Jessica Louise Hodges 2007

All Rights Reserved

MULTI-YEAR SEARCH FOR A DIFFUSE FLUX OF MUON NEUTRINOS WITH AMANDA-II

Jessica Louise Hodges

Under the supervision of Professor Albrecht Karle

At the University of Wisconsin — Madison

Neutrinos are valuable messengers that are expected to help answer fundamental questions about our Universe, including the origin of cosmic rays and the nature of cosmic accelerators. Neutrino astrophysics may even open a window to processes or objects we have never yet imagined. The AMANDA-II detector was constructed to search for and identify distant neutrino sources with non-thermal components. This analysis of AMANDA-II data collected between February 2000 and November 2003 searches for a diffuse flux of TeV - PeV muon neutrinos from unresolved astrophysical sources across the entire northern sky. Since astrophysical neutrinos are expected to have a harder energy spectrum than the atmospheric muon and neutrino backgrounds, an energy-dependent parameter was used to separate the signal and background event classes. No excess of events was seen in the data over the expected background, therefore upper limits were placed on the diffuse flux of muon neutrinos based on several different astrophysical neutrino models. Because of their harder spectra, prompt atmospheric neutrino predictions were also tested and constrained.

Albrecht Karle (Adviser)

Acknowledgments

This work would not have been possible without the support of many people. You encouraged and guided me. You corrected me when I was wrong and supported me when I was right. You listened. You comforted. You laughed with me. For this, I am very grateful. My thanks especially go to:

Albrecht Karle, for advising me.

Gary Hill, for always having an open door and willingly explaining it one more time.

Teresa Montaruli, Francis Halzen, Bob Morse, Paolo Desiati and Chris Wendt, for helpful discussions and support.

John Kelley and Jim Braun, my office mates, for putting up with me every day. And for listening, answering and advising. I will miss Team J!

Markus Ackermann and the Zeuthen filtering crew, for providing this data.

Tom Gaisser, Todor Stanev, Spencer Klein, Kurt Woschnagg, Marek Kowalski and Philippe Herquet, for serving as reviewers of my publication.

Amy, for listening to me talk about *cuts* and *unblindings* at the dinner table.

My parents, who told me they would always be my #1 fans.

Dan, for loving me every day.

Thank you all for believing in me!

Contents

Acknowledgments	i
1 Introduction	1
1.1 Cosmic Rays	2
2 Neutrino Astronomy	6
2.1 What is a neutrino?	6
2.2 Neutrinos as Cosmic Messengers	6
2.2.1 Producing Neutrinos in Astronomical Sources	8
2.2.2 Fermi acceleration	9
2.3 Finding Astrophysical Neutrinos	12
3 Astrophysical Neutrino Models and Limits	14
3.1 $\Phi \propto E^{-2}$ Neutrino Models	14
3.1.1 Waxman-Bahcall Upper Bound	16
3.1.2 Nellen, Mannheim and Biermann Model	17
3.1.3 Becker, Biermann and Rhode Model	17
3.1.4 Mannheim, Protheroe and Rachen Upper Bound for Thick Sources	18

	iii
3.2	Neutrino Spectra Different than $\Phi \propto E^{-2}$ 18
3.2.1	Stecker, Done, Salamon and Sommers AGN Core Model 18
3.2.2	Mannheim, Protheroe and Rachen Upper Bounds for Thin Sources 19
3.2.3	Mannheim, Protheroe and Rachen Upper Bound for Neutrinos from AGN Jets 20
3.2.4	Loeb and Waxman Starburst Model 20
3.3	Existing Astrophysical Neutrino Upper Limits 21
4	Atmospheric Neutrinos 24
4.1	Conventional vs. Prompt Atmospheric Neutrinos 24
4.2	Prompt Atmospheric Neutrino Models 28
4.3	Existing Prompt Neutrino Upper Limit 33
5	Neutrino Detection with AMANDA 34
5.1	Search Method 34
5.2	AMANDA Detection Principle 36
5.3	AMANDA Detector 38
5.3.1	AMANDA Coordinate System 41
5.4	Optical Properties of South Pole Glacial Ice 43
6	Preparation of the 2000 - 2003 Sample 47
6.1	Livetime and Triggers 47
6.2	Rejection of Atmospheric Muon Background 49
6.3	Reconstruction Methods 51
6.4	Techniques to Further Improve Background Rejection 53

6.4.1	Zenith-weighted (Bayesian) Reconstruction	53
6.4.2	Removal of Electronic Crosstalk	54
6.4.3	Removal of Non-Photon Events	56
6.4.4	Paraboloid Reconstruction	57
6.4.5	Velocity of Line Fit	58
6.5	Event Simulation	58
6.5.1	Preparation of Simulated Events	60
7	Obtaining an Upgoing Neutrino Sample	63
8	Separating Atmospheric Neutrinos from Astrophysical Neutrinos	70
9	Effective Area	73
10	Systematic Uncertainty	77
10.1	Theoretical Uncertainties in the Background	78
10.1.1	Conventional Atmospheric Neutrino Flux based on the Barr <i>et al.</i> Model	78
10.1.2	Conventional Atmospheric Neutrino Flux based on the Honda <i>et al.</i> Model	78
10.1.3	Prompt Atmospheric Neutrinos	79
10.1.4	Additional Neutrino Flux Uncertainty	79
10.2	Normalizing the Simulation to the Data	81
10.3	Simulation Uncertainties	82
10.3.1	Inverted Analysis	83
10.3.2	Uncertainty in Detector Response	85

10.3.3 Relationship between Up and Downgoing Events	86
11 Results	89
11.1 Results for $\Phi \propto E^{-2}$	90
11.2 Results for Other Energy Spectra	91
11.2.1 Astrophysical Neutrino Upper Limits	94
11.2.2 Prompt Atmospheric Neutrino Upper Limits	95
12 Future Techniques for Diffuse Analyses	101
13 Conclusions	104
A Q&A for the Non-Physicist	112
A.1 What are neutrinos?	112
A.2 Why do we care about neutrinos?	113
A.3 What objects in space are we studying?	116
A.4 How we detect neutrinos?	117
A.5 How does the AMANDA detector work?	117
A.6 How does my analysis work?	118
A.7 Summing it up, plain and simple	120

Chapter 1

Introduction

For thousands of years, people have looked to the heavens and wondered what lies in the deepest regions of space. We have developed from a culture that once thought the Earth was the center of everything. Now, our imaginations cannot even begin to grasp how insignificant the Earth is in the grand scheme of the Universe. Unless the wildest science fiction stories come true, we will never be able to visit or send scientific probes to objects in distant space. In order to learn about the most distant astronomical objects, we must study the clues they send us. Cosmic particles, accelerated far from Earth, bombard our atmosphere constantly. These particles carry information that allows us to better understand the Universe.

The earliest studies of the heavens focused on easily observable objects: the Sun, Moon and stars. After centuries of questions about the Sun, the particle interactions that control its burning mechanism are now fairly precisely understood. Now our focus stretches beyond the stars. We hope to understand the interactions occurring between particles in objects in distant galaxies. Neutrinos were a key component in understanding how the Sun burns and they promise to be equally informative about processes occurring in other galaxies.

This analysis focuses on the search for astrophysical neutrinos from distant (non-solar) sources. First, I will discuss cosmic rays and why neutrino studies are needed to answer the most fundamental questions about our Universe. Then I will address the neutrino production models in astrophysical sources. The last several chapters will describe the search for astrophysical neutrinos using the AMANDA-II detector located at the South Pole.

1.1 Cosmic Rays

Cosmic rays are charged particles traveling through space at very high energies. Most of the cosmic rays are protons ($\sim 85\%$) [1]. About 12% of the cosmic rays are helium nuclei, while other heavier nuclei make up about 1%. Electrons make up the final 2%. Man-made particle accelerators are limited in size and hence limited in the particle energies that they can achieve. The world's biggest accelerator, the Large Hadron Collider (LHC), is currently being constructed at CERN and is expected to accelerate protons to collision energies of about 14 TeV [2]. Cosmic rays, on the other hand, are some of nature's most energetic particles. They have been observed with energies as high as 10^{20} eV. This is seven orders of magnitude larger than the LHC! This gives rise to interesting questions: what astrophysical sources are producing the flux of cosmic rays and how are the particles accelerated to such large energies? Cosmic ray and neutrino astrophysics are closely related since accelerated cosmic rays will sooner (at the acceleration source) or later (at another target) interact and produce neutrinos.

The cosmic ray energy spectrum follows an inverse power law over many orders of magnitude. The differential flux is described by the following equation [3]:

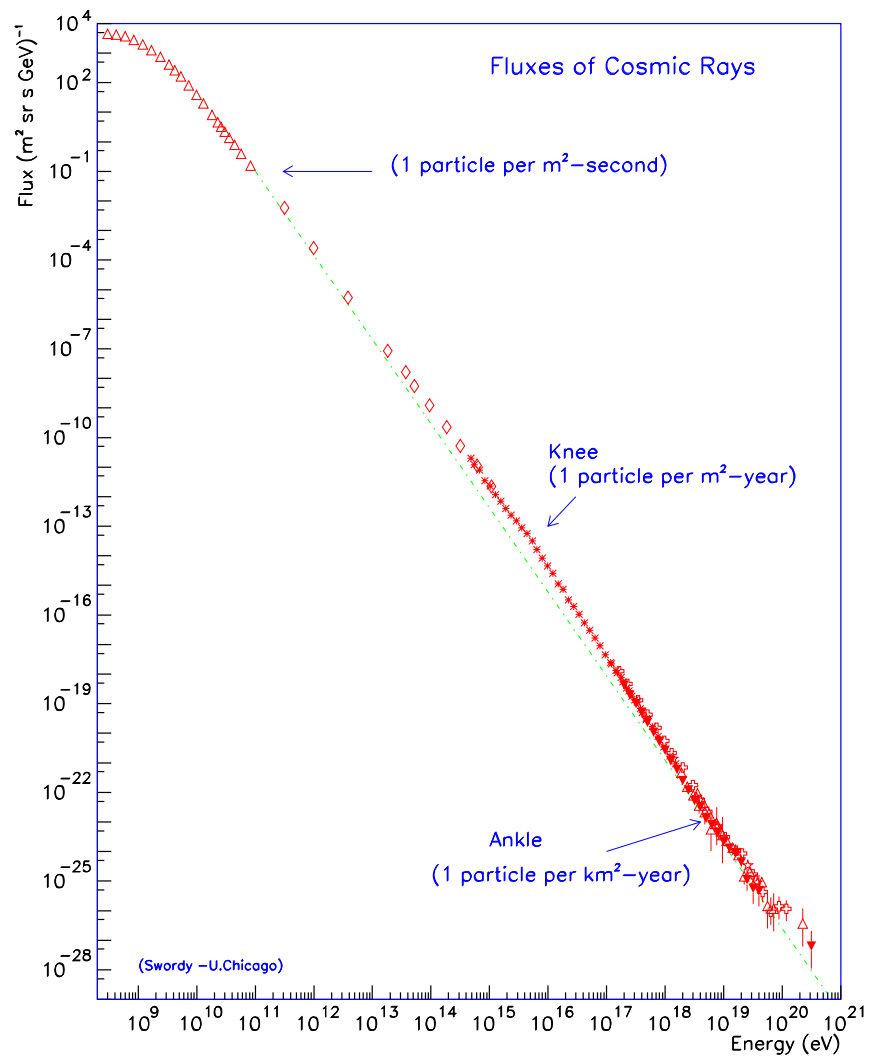


Figure 1.1: The cosmic ray spectrum. (Image credit: Swordy, University of Chicago).

$$\frac{dN}{dE} \propto E^{-(\gamma+1)} . \quad (1.1)$$

Several features in the cosmic ray spectrum are worth noting. At energies less than about 10^9 eV, the flux is much lower than predicted by the power law. This effect is known as solar modulation. Before arriving at Earth, cosmic rays must travel through the solar wind. Low energy particles have a more difficult time traveling through this wind due to disturbances in the magnetic field [1]. Hence, the low energy flux of cosmic rays at Earth is attenuated.

The *knee* is the region around 4×10^{15} eV where a slope change occurs [3, 4]. At lower energies than the knee, $\gamma \sim 1.7$. However, at energies above the knee, $\gamma \sim 2.2$ [3]. At 5×10^{18} eV, the slope changes again at the *ankle* and returns to $\gamma \sim 1.7$. In the highest observed regions of the spectrum, a sudden cutoff in the cosmic ray flux is expected at 5×10^{19} eV. At the Greisen-Zatsepin-Kuzmin (GZK) limit, cosmic rays are at the threshold energy to interact with cosmic microwave background (CMB) photons. These interactions produce pions. Current measurements of the cosmic ray flux in the energy region above 10^{19} eV are conflicting, so the existence of the GZK cutoff will need to be verified by the next generation of ultra high energy cosmic ray experiments.

For energies below 10^{15} eV (the knee), supernova remnants (SNR) in our galaxy are considered the most likely source to accelerate cosmic rays [5]. These non-thermal sources are suspected because they follow power law spectra. They are also powerful enough to accelerate the particles and have chemical abundances similar to the cosmic rays [5]. Above 10^{15} eV, it is likely the cosmic rays come from outside of the galaxy.

Many current theories predict mechanisms for particle acceleration in different astrophysical objects. Because the models include both charged particle acceleration and neutrino production, the search for astrophysical neutrinos is linked to the question of how cosmic rays of such high energies can be formed. This analysis focuses on the search for neutrinos from distant sources.

Chapter 2

Neutrino Astronomy

2.1 What is a neutrino?

Neutrinos are very tiny, chargeless particles from the lepton family. They interact via the weak force. There is a corresponding neutrino for each of the three lepton flavors: electron, muon and tau. From their inception, neutrinos were thought to be massless particles, but recent evidence from neutrino oscillations experiments such as SNO (Sudbury Neutrino Observatory) and Super-Kamiokande suggests otherwise. Neutrino oscillations (where neutrinos transform from one flavor to another) have been observed, which can only happen if neutrinos have non-zero mass and they are not degenerate.

2.2 Neutrinos as Cosmic Messengers

One of the ultimate goals of astrophysics is to piece together information from cosmic ray and neutrino telescopes and telescopes measuring electromagnetic radiation (gamma-ray, optical, infrared, radio, X-ray) into a coherent picture of the inner workings of distant astrophysical objects. Questions about cosmic rays, gamma rays

and neutrinos all seem to be connected. Each of these three types of particles can provide valuable clues and there are advantages and disadvantages to each type of study.

Photons are the traditional way of studying the sky. The first astronomers studied the heavens based on the light that they could see with their eyes. It is, of course, possible to study photons in other ranges of the electromagnetic spectrum, for instance, the radio, infrared, ultraviolet, X-ray and gamma-ray regions. Despite the fact that photons are abundant and easy to observe, photons do not lend themselves to high energy studies because of their limited distance range. High energy photons tend to be absorbed by matter before they can reach the Earth.

Cosmic rays are easily detected. However, at most energies (including the TeV – PeV energy range of this analysis), cosmic rays do not carry directional information because charged particles are deflected by magnetic fields. At ultra high energies ($\gtrsim 10^{19}$ eV), galactic cosmic rays experience only a small deflection from their original direction and hence point backward to their source [6].

Neutrinos are chargeless and hence are not deflected by magnetic fields. Since they travel in straight lines, they carry directional information about their point of origin. Unfortunately, detecting a neutrino event is rather challenging. Neutrinos are weakly-interacting particles with very small cross-sections.

Neutrinos are a source of information about the physical processes occurring in cosmic accelerators. First, we would like to identify what types of sources are capable of producing the highest energy cosmic rays. Theories suggest that these ultra high energy particles are being accelerated in processes that should also include neutrino

production. If neutrinos originate from the direction of a specific source, we know that hadronic interactions (mainly pp and $p\gamma$) are occurring in that source. In that case, it is possible that protons are being accelerated up to the ultra high energies observed.

Gamma ray telescopes, such as HESS (High Energy Stereoscopic System) [7] and MAGIC (Major Atmospheric Gamma Ray Imaging Telescope) [8], have identified many gamma-ray sources across the sky. It is hoped that neutrino production can also be linked to these same sources.

2.2.1 Producing Neutrinos in Astronomical Sources

Active galactic nuclei (AGN), gamma ray bursts (GRBs), supernova remnants (SNR) and starburst galaxies are among the astronomical objects that could be producing neutrinos. They are all considered possible sources in which particles are accelerated to high energies through shock acceleration processes. The most widely accepted model of shock acceleration is first order Fermi acceleration, which will be described later in this chapter. First, it is important to discuss what particles must be present and what interactions must occur in order to produce neutrinos.

Hadronic proton-proton (pp) and proton-photon ($p\gamma$) interactions are expected to occur in astrophysical sources. These interactions create charged and neutral pions and kaons. As can be seen in the following equations, neutrinos result from charged pion and kaon decay. If neutrino and γ -ray production can be identified in the same sources, that would be strong evidence that pp and $p\gamma$ interactions like those described below are occurring in those astrophysical sources. Note that pions and kaons follow similar decay chains, so only the pion chain is shown. Charged pions (kaons) create neutrinos, but neutral pions (kaons) decay into two gamma rays.

$$\begin{aligned}
\pi^+ &\rightarrow \mu^+ + \nu_\mu \rightarrow (e^+ + \nu_e + \bar{\nu}_\mu) + \nu_\mu \\
\pi^- &\rightarrow \mu^- + \bar{\nu}_\mu \rightarrow (e^- + \bar{\nu}_e + \nu_\mu) + \bar{\nu}_\mu \\
\pi^0 &\rightarrow \gamma\gamma
\end{aligned}
\tag{2.1}$$

The flavor ratio at the time of the neutrino production in the source is expected to be $\nu_e:\nu_\mu:\nu_\tau = 1:2:0$. (ν and $\bar{\nu}$ are both counted in the ν flux as it is labelled here.) Since neutrinos can change flavors, or oscillate, the expected flavor ratio of the astrophysical neutrinos at the detector is not 1:2:0; $\nu_\mu - \nu_\tau$ mixing leads to a 1:1:1 flavor ratio at Earth [9]. However, Kashti and Waxman [10] have pointed out that at high energies ($E \gtrsim 100$ TeV) μ decay in the source region becomes suppressed. This results in a flavor ratio at Earth of 1:1.8:1.8.

2.2.2 Fermi acceleration

First order Fermi acceleration describes the process in which particles are accelerated in strong shocks [1, 11]. A shock wave occurs as gas or particles are flowing (or exploding) out of an object and travel faster than the speed of sound in the medium. As particles pass through a shock wave, a number of conservation laws must be upheld. The conservation of mass, energy flux, and momentum flux across the shock all allow a series of relations to be derived about the particles. In the case of a strong shock (Mach number $\gg 1$),

$$\frac{\rho_2}{\rho_1} = \frac{(\gamma_h + 1)}{(\gamma_h - 1)}
\tag{2.2}$$

where ρ is the gas density and γ_h is the ratio of specific heats. For a monatomic

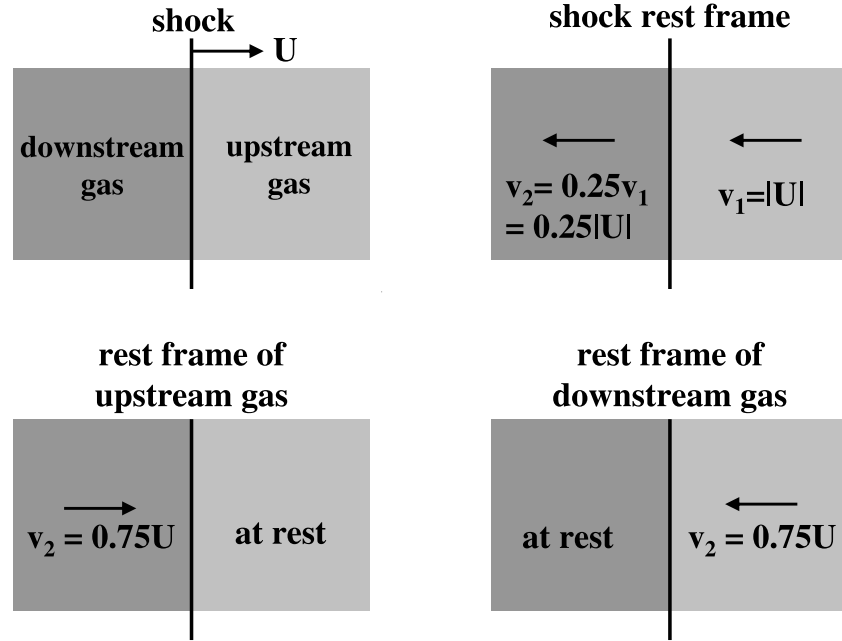


Figure 2.1: Fermi acceleration from different points of view. In the frame of reference of the upstream and downstream gas, the particles gain energy as they cross the shock.

gas, $\gamma_h = \frac{5}{3}$.

This leads to the relation

$$\frac{\rho_2}{\rho_1} = \frac{8/3}{2/3} = 4 \quad (2.3)$$

which will be used later in further calculations.

Because of conservation of mass across the shock wave, $\rho_1 v_1 = \rho_2 v_2$, the velocities of the gases on either side of the shock are related by the following:

$$v_2 = \frac{1}{4} v_1. \quad (2.4)$$

Consider a shock wave travelling outward from an astrophysical object (Figure

2.1 upper left). Its speed of travel is U . To move into the reference frame of the shock (Figure 2.1 upper right), add $-U$ to either side of the shock. The upstream material comes at the shock (at rest) at a speed $v_1 = -U$. Using equation 2.4, the downstream material moves away from the shock at $v_2 = -0.25v_1 = -0.25U$.

To move into the reference frame of the upstream gas (Figure 2.1 lower left), add U to the either side of the shock rest frame. The downstream material went from moving at $.25U$ to the left to $0.75U$ to the right.

Similarly, to move into the reference frame of the downstream gas (Figure 2.1 lower right), add $0.25U$ to both sides in the shock's rest frame. The upstream material now has a speed $-U+0.25U = -.75U$. Remarkably, no matter which direction it comes from, a particle always approaches the shock at $0.75U$.

When a particle crosses the shock, it always gains energy, independent of the direction it is crossing. Furthermore, particles may cross the shock multiple times. They gain an amount of energy, β , every time they cross. Assuming that a particle crosses a shock k times, its energy, E , will be:

$$E = \beta^k E_o \quad (2.5)$$

Assuming P is the probability of crossing the shock, the number of particles with energy E ($E > E_o$) is:

$$N = P^k N_o \quad (2.6)$$

where N_o is the number of particles with the original energy E_o . Equations 2.5 and 2.6 can be combined as:

$$\frac{N}{N_o} = \left(\frac{E}{E_o}\right)^{\frac{\ln P}{\ln \beta}} \quad (2.7)$$

The spectral index, γ , of the charged particles is defined as

$$\gamma = \frac{\ln P}{\ln \beta}. \quad (2.8)$$

Equation 2.7 suggests that $N \sim E^\gamma$, hence the differential energy spectrum is

$$\frac{dN}{dE} \sim E^{\gamma-1}. \quad (2.9)$$

A few assumptions can be used to determine the value of the spectral index, γ : the energy gain β is proportional to $\frac{v_1-v_2}{c}$, and the probability of crossing the shock is proportional to $\frac{v_1}{c}$. The detailed calculation is not shown here, but these assumptions lead to the conclusion that $\gamma = -1$. Hence, the predicted energy spectrum for first order Fermi acceleration is:

$$\frac{dN}{dE} \sim E^{-2}. \quad (2.10)$$

This generic energy spectrum is used as a common benchmark in the search for astrophysical neutrinos.

2.3 Finding Astrophysical Neutrinos

In the early 1960s, it was realized that neutrinos should play an important role in accelerators of cosmic rays and that we could detect neutrinos on Earth. When neutrinos interact with matter, the resulting Cherenkov radiation can be detected in

a transparent medium. K. Greisen, F. Reines and M.A. Markov and I.M. Zheleznykh pioneered the design of future astrophysical neutrino detectors based on this principle.

In 1960, K. Greisen wrote [12]:

Let us now consider the feasibility of detecting the neutrino flux. As a detector, we propose a large Cherenkov counter, about 15 m in diameter, located in a mine far underground. The counter should be surrounded with photomultipliers to detect the events, and enclosed in a shell of scintillating material to distinguish neutrino events from those caused by μ mesons. Such a detector would be rather expensive.... About 500 reactions per year would be expected from neutrinos produced in the atmosphere, but these would have a steeper energy spectrum and a different angular distribution from that of the primary neutrinos, with a maximum in the horizontal direction, where the longer path length in the atmosphere permits more of the mesons to decay. The atmospheric neutrinos would serve to verify the neutrino cross section and calibrate the apparatus.

Also in 1960, F. Reines predicted that, at least half the time, neutrinos would continue in the same direction as the pion to within 10% [13]. As a result, he predicted studying the astrophysical neutrino flux by building a detector that consisted of “a water target in a white container at the end of which are located a few hundred 5-in. photomultiplier tubes.”

M.A. Markov and I.M. Zheleznykh stated in 1961 [14], “All known particles with the exception of neutrinos are absorbed by scores of kilometres of the substance and thus are entirely screened by the planet...”

These ideas became the foundation of a new field: neutrino astrophysics.

Chapter 3

Astrophysical Neutrino Models and Limits

With the field of neutrino astronomy wide open to speculation, many models have been developed to predict the neutrino flux from extraterrestrial sources over a wide energy range. Astrophysical neutrino models come with various shapes and normalizations. Some models have been normalized based on the extragalactic gamma ray background, while others try to pinpoint the neutrino flux based on ultra high energy cosmic ray, X-ray, or radio measurements

Even if no extraterrestrial signal is detected, upper limits on the neutrino flux can be determined that rule out or constrain existing neutrino production theories. Some models predict an energy spectral shape and normalization, while other predictions are only upper bounds.

3.1 $\Phi \propto E^{-2}$ Neutrino Models

As mentioned previously, $\Phi \propto E^{-2}$ is a generic spectrum predicted by first order Fermi acceleration. A number of theories have been developed based on this spectral shape. A common benchmark in neutrino astronomy is the Waxman-Bahcall (WB) upper bound [15, 16, 17], which assumes the $\Phi \propto E^{-2}$ spectrum. Current detectors

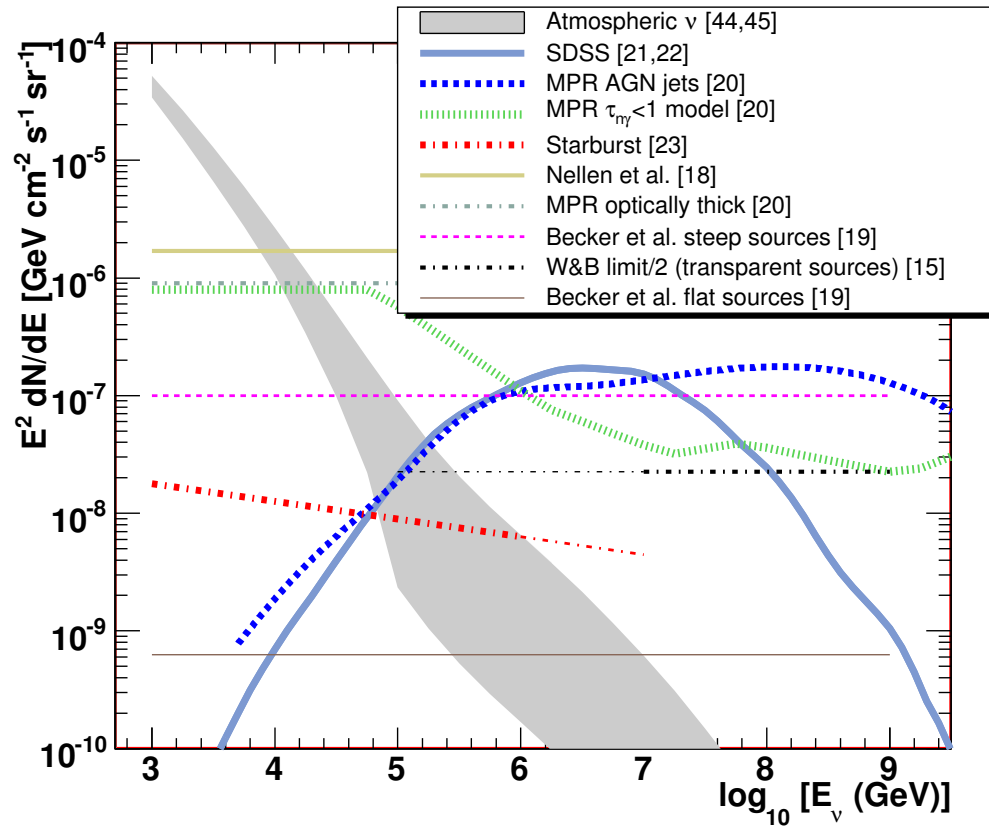


Figure 3.1: Astrophysical neutrino models span many orders of magnitude and have varying energy spectra.

are striving to attain the sensitivity of the WB bound. Astrophysical neutrino models and bounds developed by Nellen *et al.*, Becker *et al.* and MPR all have a $\Phi \propto E^{-2}$ spectral shape.

3.1.1 Waxman-Bahcall Upper Bound

The Waxman-Bahcall upper bound [15, 16, 17] assumes that cosmological sources of protons have a $\Phi \propto E^{-2}$ injection spectrum. When protons interact with the radiation field of a source, charged and neutral pions are produced in equal amounts. Neutral pions do not decay into neutrinos. When a charged pion decays, half of the energy of the pion is carried by the muon neutrinos and antineutrinos. The neutrino spectrum is predicted to remain the same as that for protons, $\Phi \propto E^{-2}$.

The upper bound was determined assuming that the energy production rate of protons is

$$E_{\text{CR}}^2 \frac{d\dot{N}_{\text{CR}}}{dE_{\text{CR}}} \approx 10^{44} \text{erg Mpc}^{-3} \text{yr}^{-1}. \quad (3.1)$$

To derive the maximum value of the neutrino flux, it was assumed that protons do not lose any energy before escaping the source. The present day neutrino flux at the source was described by WB with the following equation.

$$E_{\nu}^2 \frac{dN_{\nu}}{dE_{\nu}} \approx 0.25 t_{\text{h}} E_{\text{CR}}^2 \frac{d\dot{N}_{\text{CR}}}{dE_{\text{CR}}} \quad (3.2)$$

The Hubble time, $t_{\text{h}} \approx 10^{10}$ years, is the inverse of the Hubble constant, here assumed to be about $65 \text{ km s}^{-1} \text{ Mpc}^{-1}$. Using the relation $\Phi_{\nu} = \frac{dN}{dE} \cdot \frac{c}{4\pi \text{sr}}$ and substituting the energy production rate from equation 3.1, the maximum neutrino ($\nu_{\mu} + \bar{\nu}_{\mu}$) flux is proposed to be $\approx 1.5 \times 10^{-8} \text{ GeV cm}^{-2} \text{ s}^{-1} \text{ sr}^{-1}$.

After a correction for redshift evolution, the predicted flux is a factor of 3 higher. However, due to neutrino oscillations, the predicted muon neutrino flux is not the same at the source and the Earth. Approximately half of the muon neutrinos are expected to oscillate into other flavors. The upper bound for the flux of muon neutrinos and anti-neutrinos is $2.25 \times 10^{-8} \text{ GeV cm}^{-2} \text{ s}^{-1} \text{ sr}^{-1}$ at Earth. This upper bound only applies to optically thin sources, meaning that the optical depth τ is small.

3.1.2 Nellen, Mannheim and Biermann Model

In 1993, Nellen, Mannheim and Biermann [18] predicted an astrophysical neutrino flux of $E^2\Phi = 1.7 \times 10^{-6} \text{ GeV cm}^{-2} \text{ s}^{-1} \text{ sr}^{-1}$. They assumed that pp interactions in the source would lead to electromagnetic interactions that result in the production of neutrinos, X-rays and γ -rays. Their model for neutrino production in AGN is normalized based on X-ray background measurements by ROSAT (Röntgen Satellit). Their prediction is valid for the GeV energy region up to $4 \times 10^5 \text{ GeV}$.

3.1.3 Becker, Biermann and Rhode Model

Becker, Biermann and Rhode (2005) [19] predicted the neutrino flux from FR-II radio galaxies (steep spectrum sources) and blazars (flat spectrum sources) since AGN jets are expected to be the site of $p\gamma$ interactions that lead to neutrino production. These models were normalized by deriving the relationship between the neutrino luminosity, the disk luminosity and the radio luminosity. Each model (steep and flat) is highly dependent on what proton spectral index is used. Hence, results were presented for numerous spectra, although only the $\Phi \propto E^{-2}$ model is compared here.

For steep sources with an assumed $\Phi \propto E^{-2}$ spectrum, the predicted flux is

$\sim 1.0 \times 10^{-7} \text{ GeV cm}^{-2} \text{ s}^{-1} \text{ sr}^{-1}$ for energies up to 10^9 GeV . For flat sources and a $\Phi \propto E^{-2}$ spectrum, the model predicts a flux of $\sim 6.3 \times 10^{-10} \text{ GeV cm}^{-2} \text{ s}^{-1} \text{ sr}^{-1}$ for the same energy region.

3.1.4 Mannheim, Protheroe and Rachen Upper Bound for Thick Sources

Mannheim, Protheroe and Rachen [20] proposed several models for the astrophysical neutrino flux that will be described in more detail in the next section. They placed an upper bound on the neutrino flux for optically thick sources in which neutrons cannot escape ($\tau_{n\gamma} \gg 1$). The prediction is normalized to measurements of the extragalactic gamma ray background. The MPR upper bound for optically thick sources follows a $\Phi \propto E^{-2}$ spectrum and lies just above $10^{-6} \text{ GeV cm}^{-2} \text{ s}^{-1} \text{ sr}^{-1}$.

3.2 Neutrino Spectra Different than $\Phi \propto E^{-2}$

The following models for astrophysical neutrino production do not follow a $\Phi \propto E^{-2}$ spectrum.

3.2.1 Stecker, Done, Salamon and Sommers AGN Core Model

Stecker, Done, Salamon and Sommers (SDSS) [21, 22] developed a neutrino flux prediction based on their studies of AGN cores. The model only makes a prediction for radio-quiet AGN and was normalized to X-ray data for the AGN luminosity function and redshift information collected by ROSAT. In 2005, Stecker published a revision to the original prediction, citing new observational evidence. The original model assumed that 100% of the X-ray background was nonthermal radiation from AGN. However, it is now shown that AGN emit mainly thermal radiation. For the galactic black hole

source Cyg X-1, the energy spectrum can be explained if 90% of the power contributes to a thermal electron distribution while 10% of the power goes to nonthermal γ -rays. Instead of assuming 100% of the AGN output was nonthermal, now the SDSS model assumes only 10%. This leads to a reduction in the SDSS model by a factor of 10. In addition, neutrino oscillations were confirmed after the SDSS model was issued. This means that the muon neutrino flux should decrease by a factor of two by the time it is detected on Earth. After the Stecker revision in 2005, the predicted flux is a factor of 20 smaller.

3.2.2 Mannheim, Protheroe and Rachen Upper Bounds for Thin Sources

MPR [20] based their models for astrophysical neutrino production on the observed cosmic ray spectrum. Instead of using the $\Phi \propto E^{-2}$ spectrum assumed by Waxman and Bahcall, they assumed a cosmic ray injection spectrum that is consistent with the observable cosmic ray flux. Based on results from Havarah Park, Akeno Giant Air Shower Array (AGASA), Fly's Eye, Yakutsk and the KASCADE air shower experiment, they assumed an extragalactic cosmic ray spectrum of the form

$$N_{p,obs}(E) = 0.8 \times (E/\text{GeV})^{-2.75} \text{ cm}^{-2}\text{s}^{-1}\text{sr}^{-1}\text{GeV}^{-1} \quad (3.3)$$

for energies between 3×10^6 GeV and 10^{12} GeV. To form the upper bound for optically thin sources, the cosmic ray spectrum was calculated in small energy ranges characterized by an energy E_{max} between 10^6 and 10^{12} GeV. Each of these cosmic ray proton spectra was normalized such that the peak of the distribution for each E_{max} reached the extragalactic cosmic ray spectrum in equation 3.3. Since the cosmic ray and gamma ray outputs are correlated, the cosmic ray normalizations also had

to agree with the observed gamma ray background. For that reason, the peak of the normalized curve for $E_{max} = 10^6$ falls below the observed cosmic ray spectrum so as not to overproduce gamma rays. The neutrino spectrum was then derived from each normalized (and maximized) cosmic ray spectrum for the particular values of E_{max} . An envelope was drawn that connects the peak of each neutrino spectrum and this represents the MPR upper bound for neutrinos from sources that are optically thin to neutrons.

3.2.3 Mannheim, Protheroe and Rachen Upper Bound for Neutrinos from AGN Jets

MPR also projected an upper bound on the flux of neutrinos from AGN jets. They followed the same procedure just described to normalize the neutrino spectrum to the observed cosmic ray flux. For this calculation, they used the same generic cosmic ray and neutrino production spectra as were used in the determination of the thin sources upper bound. In this case, they fixed the value of $E_{max} = 10^{11}$ GeV. The break energy (E_b) was allowed to vary between 10^7 and 10^{11} GeV. The upper bound is the maximized superposition of the spectra with different input parameters, E_b .

3.2.4 Loeb and Waxman Starburst Model

Loeb and Waxman [23] proposed a neutrino production model for starburst galaxies. Since evidence suggests that the magnetic field in starburst galaxies is 100 times larger than in the intergalactic medium, the protons lose all of their energy to pion production before they escape from the source. The flux prediction was normalized based on the observed synchrotron radio flux of electrons. The predicted

energy spectrum was derived by considering both the cosmic ray proton spectrum on Earth ($\Phi \propto E^{-2.75}$) and the confinement time in the source ($t \propto E^{-0.6}$). The predicted flux is $E_\nu^2 \Phi_\nu^{\text{SB}} \approx 10^{-7} (E_\nu/1 \text{ GeV})^{-0.15 \pm 0.1} \text{ GeV cm}^{-2} \text{ s}^{-1} \text{ sr}^{-1}$. However, the authors felt that large uncertainties should be taken into account and hence the model encompasses a large region on a neutrino flux plot due to uncertainties in the proton spectrum, the confinement time spectral index, and the location of the knee in the cosmic ray spectrum.

3.3 Existing Astrophysical Neutrino Upper Limits

The most widely tested spectrum by neutrino experiments is the generic $\Phi \propto E^{-2}$ spectrum. Fréjus, MACRO, Baikal and AMANDA have all published upper limits on the diffuse flux of neutrinos with this energy spectrum.

A precursor to this muon neutrino analysis was conducted with data collected in 1997 by the AMANDA-B10 detector [24]. (In 1997, the AMANDA detector consisted of 10 sensor strings, a subset of the 19 strings in the final AMANDA-II configuration.) This analysis focused on the $\Phi \propto E^{-2}$ spectrum, but also set upper limits on several other spectral shapes.

Other AMANDA analyses have focused on the search for a diffuse flux of neutrinos using particle showers or cascades [25] instead of muon neutrinos. Cascades are caused by ν_e and ν_τ charged current interactions and all-flavor neutral current interactions in the ice near the detector. Upper limits from these analyses constrain the flux of neutrinos of all flavors, not just muon neutrinos.

The Fréjus [26], MACRO [27], and Baikal [28]) experiments have set upper limits on the flux of astrophysical neutrinos in the same energy region as this analysis (TeV

Experiment	Upper Limit [GeV cm ⁻² s ⁻¹ sr ⁻¹]	Energy Range log ₁₀ [E _ν (GeV)]
<i>Muon neutrinos only</i>		
Fréjus [26]	5.0 × 10 ⁻⁶	~3.4
MACRO [27]	4.1 ± 0.4 × 10 ⁻⁶	4.0 – 6.0
AMANDA-B10 [24]	8.4 × 10 ⁻⁷	3.8 – 6.0
<i>All neutrino flavors</i>		
Baikal [28]	8.1 × 10 ⁻⁷	4.3 – 7.7
AMANDA-B10 [29]	0.99 × 10 ⁻⁶	6.0 – 9.5
AMANDA-II [25]	8.6 × 10 ⁻⁷	4.7 – 6.7

Table 3.1: Upper limits for the diffuse flux of extraterrestrial neutrinos as reported by a number of experiments. The first four analyses only constrain the flux of $\nu_\mu + \bar{\nu}_\mu$, while the last three constrain the total neutrino flux, $(\nu_e + \bar{\nu}_e + \nu_\mu + \bar{\nu}_\mu + \nu_\tau + \bar{\nu}_\tau)$.

- PeV). Published upper limits from these experiments assuming a $\Phi \propto E^{-2}$ spectrum are summarized in Table 3.1. Depending on the detector and the specific analysis, the reported upper limit constrains either the muon neutrino flux or the all-flavor neutrino flux. Upper limits obtained from all-flavor analyses are not directly comparable to ν_μ upper limits. However, for a wide range of neutrino production models and oscillation parameters, the flavor flux ratio at Earth can be approximated as 1:1:1 [9]. In that case, either a single-flavor limit can be multiplied by three and compared to an all-flavor result, or an all-flavor limit can be divided by three and compared to a single-flavor result.

The Baikal experiment has placed limits on models with spectra other than $\Phi \propto E^{-2}$ [28], which are compared to the results from the 1997 AMANDA-B10 analysis in Table 3.2.

In this analysis, nine different spectral shapes are tested, including the search

Experiment	Upper Limit	
	SDSS*	MPR AGN Jets
Baikal [28]	$2.5 \cdot \Phi_{\text{SDSS}}$	$4.0 \cdot \Phi_{\text{MPR}}$
AMANDA-B10 [29]	$23.2 \cdot \Phi_{\text{SDSS}}$	not tested

* = model lowered by factor of 10 by Stecker in 2005

Table 3.2: Upper limits for the diffuse flux of extraterrestrial neutrinos from spectra different than $\Phi \propto E^{-2}$. Note that all upper limits on the SDSS flux are adjusted to take into account the 2005 revision by Stecker.

for prompt neutrinos from the decay of charmed particles described in Chapter 4. Since this analysis is optimized on energy-dependent parameters, the optimization was performed individually for each energy spectrum.

Chapter 4

Atmospheric Neutrinos

Atmospheric muons and neutrinos form the primary background for the search for astrophysical neutrinos. When cosmic rays interact in Earth's atmosphere, muons and neutrinos are among the particles that are formed. While the so-called atmospheric muons are the largest background to the search for astrophysical neutrinos, they are also the easiest background to remove since they are unable to travel all the way through the Earth. On the other hand, both atmospheric neutrinos and the desired astrophysical signal can approach the detector from any direction. It is important to thoroughly understand this important background.

4.1 Conventional vs. Prompt Atmospheric Neutrinos

When cosmic rays hit the atmosphere, interactions lead to the generation of many types of particles. Two different event classes are used to describe the resulting atmospheric muons and neutrinos: conventional and prompt.

The *conventional* atmospheric muon and neutrino fluxes are the product of pion and kaon decays in the atmosphere. Pion and kaon decays occur via similar processes, hence only the pion decay chain is shown below:

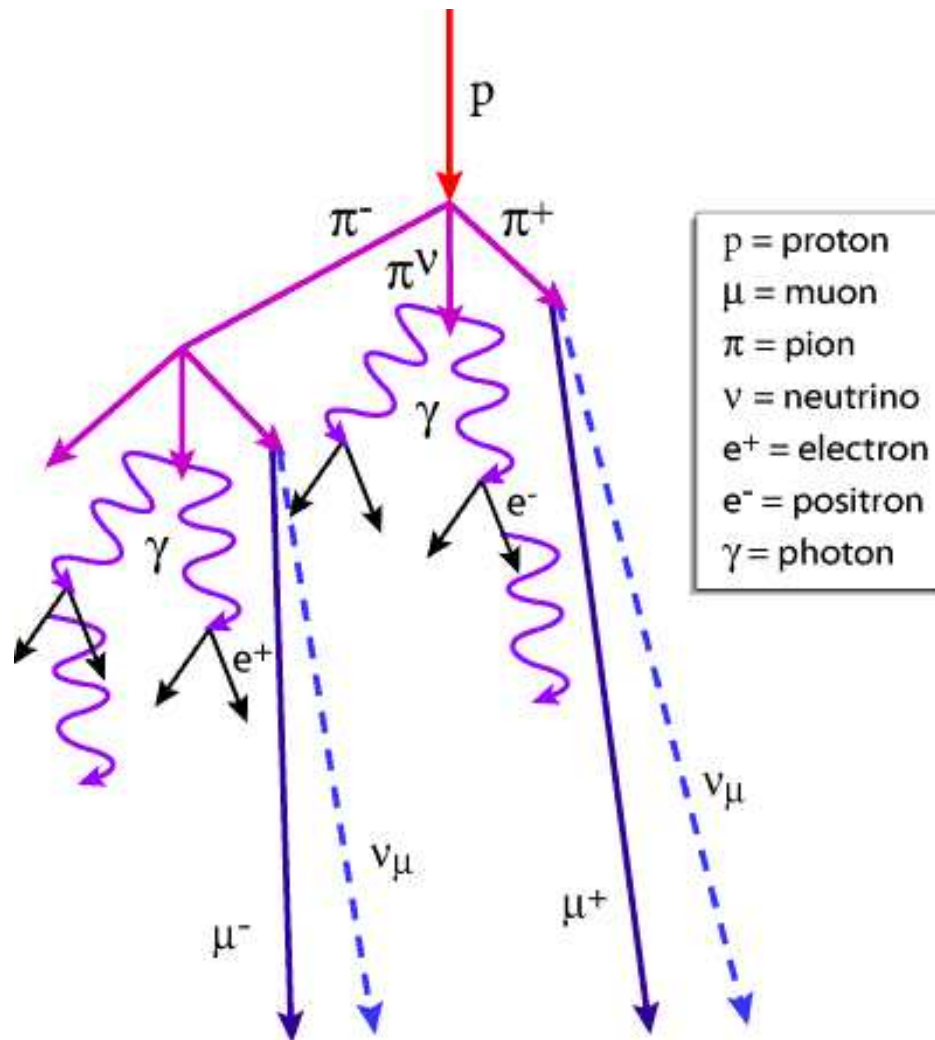


Figure 4.1: Cosmic ray interactions in the atmosphere. (Image credit: Milagro)

$$\pi^\pm \rightarrow \mu^\pm + \nu_\mu(\bar{\nu}_\mu) \quad (4.1)$$

$$\mu^\pm \rightarrow e^\pm + \nu_e(\bar{\nu}_e) + \bar{\nu}_\mu(\nu_\mu) \quad (4.2)$$

The second class of events results from the semileptonic decay of charm particles, meaning mesons that contain either a charm (c or \bar{c}) quark. Since these charm particles decay quickly before they can lose much energy, the resulting neutrinos are called *prompt* neutrinos. The following D meson and Λ_c particle decays are among the most common semileptonic charm decays [30, 31].:

$$D^+ \rightarrow \bar{K}^0 + \mu^+ + \nu_\mu \quad (4.3)$$

$$D^+ \rightarrow \bar{K}^0 + e^+ + \nu_e \quad (4.4)$$

$$\Lambda_c^+ \rightarrow \Lambda_0 + \mu^+ + \nu_\mu \quad (4.5)$$

The total atmospheric neutrino flux is dependent on the critical energies of the particles that can decay into neutrinos, ϵ_{crit} , where ϵ_{crit} is the energy for which the decay length and interaction length are equal [32]. As the energy increases, it is more likely that a particle will interact rather than decay. If interactions take place instead of decays, no neutrinos are immediately produced. Since the critical energies for pions, kaons and charm particles are all different, each of these neutrino decay sources is dominant at different energies.

Particle	ϵ_{crit} (GeV)
μ^\pm	1.0
π^\pm	115
K^\pm	850
D^\pm	3.8×10^7
D^0, \bar{D}^0	9.6×10^7
D_s^\pm	8.5×10^7
Λ_c^+	2.4×10^8

Table 4.1: Critical energy for different particles.

$$\epsilon_{\text{crit}} = \frac{mc^2}{c\tau} h_o \quad (4.6)$$

The critical energy, ϵ_{crit} , is calculated from the particle's rest energy mc^2 and the mean life time τ . The constant h_o comes from the assumption of an isothermal atmosphere [32].

Table 4.1 lists the critical energy of several particles that contribute muons and neutrinos to the atmospheric flux when they decay. Pions and kaons have critical energies of 115 and 850 GeV, respectively. However, the critical energy for charm mesons is approximately five orders of magnitude larger.

Below ϵ_{crit} , particles are more likely to decay than interact and the secondary particles will have the same energy spectrum as the parent. However, for particle decays above the critical energy, the energy spectrum of the secondary particles increases by one over the spectral index of the parent [33]. For instance, pions less than 115 GeV (and their decay products) will follow a $\Phi \propto E^{-2.7}$ spectrum just as the cosmic rays that created them. However if the energy is above ϵ_{crit} , the resulting neutrinos have a $\Phi \propto E^{-(2.7+1)}$ spectrum.

In the TeV – PeV energy range of this analysis, conventional atmospheric neutrinos come from particle decays that occur above the critical energy. As a result, conventional atmospheric neutrinos follow a $\Phi \propto E^{-3.7}$ spectrum for the entire energy region covered by this analysis. Atmospheric neutrinos from the decay of charm particles are still below ϵ_{crit} and hence follow a $\Phi \propto E^{-2.7}$ spectrum. Somewhere above 850 GeV (the kaon critical energy), charm particle decays become the dominant source of atmospheric muons and neutrinos.

Many parameters go into the calculation of the atmospheric neutrino flux and the models are highly subjective. Every model makes different assumptions about the input parameters for calculating the prompt flux. Since the particle interactions have branching ratios that indicate that neutrinos are not always formed, Monte Carlo simulations are the best way to predict the atmospheric neutrino flux. The conventional atmospheric neutrino simulation will be discussed in detail in Chapter 6. Since prompt neutrinos dominate over the conventional atmospheric neutrino flux at high energy because of their harder spectrum, it is possible to treat prompt atmospheric neutrinos as *signal* and search for these events in the detector.

4.2 Prompt Atmospheric Neutrino Models

There is a great deal of uncertainty in the prompt atmospheric neutrino flux since particle accelerators are not energetic enough to probe the energy region relevant to charm production in the atmosphere. As a result, models predict prompt neutrino fluxes that vary widely over several orders of magnitude. There are many different parameters that go into each model, for instance the primary spectral index, γ , the critical energy, and the interaction and decay lengths.

The flux of secondary charm particles, Φ_i , can be described by an equation with three terms [33]:

$$\frac{d\Phi_i(x, E_i, \theta)}{dx} = -\frac{1}{\lambda_i}\Phi_i(x, E_i, \theta) - \frac{\epsilon_{\text{crit}}}{E_i x}\Phi_i(x, E_i, \theta) + \int_{E_i}^{\infty} \frac{1}{\lambda_N}\Phi_N(x, E_N, \theta)\frac{dW^{iN}}{dE_i}dE_N. \quad (4.7)$$

In Equation 4.7, i stands for the type of charm particle, for instance, D^\pm , D^0 , Λ_c . The flux is dependent on three parameters: x is the depth of the atmosphere that has been penetrated in g/cm^2 , E_i is the particle energy and θ is the angle of the particle's approach. This equation can be simplified by considering each of the three terms separately.

The first term in Equation 4.7 represents the loss of charm particles due to interactions in the air. The nuclear interaction mean free path is λ_i .

The second term in Equation 4.7 represents charm particle decay. This term is directly proportional to the critical energy, ϵ_{crit} .

The last term accounts for the production of new charm particles throughout the shower development in the atmosphere. The initial nucleon flux is Φ_N . The nucleonic interaction length, λ_N is the mean free path of nucleons in the atmosphere [30].

$$\lambda_N = \frac{Am_p}{\sigma_{in}^{N-air}} \quad (4.8)$$

In equation 4.8, A is the atomic number for an air nucleus (on average, $A=14.5$). The proton mass is m_p . The total inelastic cross section for nucleon (N) and air interactions is σ_{in}^{N-air} .

The final parameter in the third term of equation 4.7 is $\frac{dW^{iN}}{dE_i}$. This is the energy

distribution of the secondary charm particles that are produced.

The production of charm particles in the atmosphere is often described by a parameter called the Z-moment. It is related to the charm production cross section and varies greatly between the different prompt atmospheric neutrino models. Before defining the Z-moment, one further parameter must be described. x_F , also called Feynman x, is the fractional momentum that the charm particle receives from its parent. The Z-moment is defined as [30]:

$$Z_{Ni}(\gamma) = \int_0^1 x_F^\gamma \frac{dW^{Ni}}{dx_F} dx_F \quad (4.9)$$

The large variation in the Z-factor across the different models leads to the wide spread in prompt atmospheric neutrino predictions. A few of the models that were used in this analysis are described below.

The **Martin GBW** (Golec-Biernat and Wüsthoff) [34] model utilizes perturbative quantum chromodynamics to predict the charm cross section. pQCD is currently the most widely accepted model of charm production based on accelerator data. This model for deep inelastic scattering includes gluon saturation effects which lower the predicted charm production cross sections. The Z-moment can be defined by the following equation with the framework of the Martin GBW prediction.

$$\sigma Z_{Ni} = \int \frac{d\sigma^c}{dx} x^{2.02} dx \quad (4.10)$$

where 2.02 is the spectral index of the incoming primary cosmic ray flux above 10^6 GeV and x is the gluon distribution of the proton. σ is the charm production cross section.

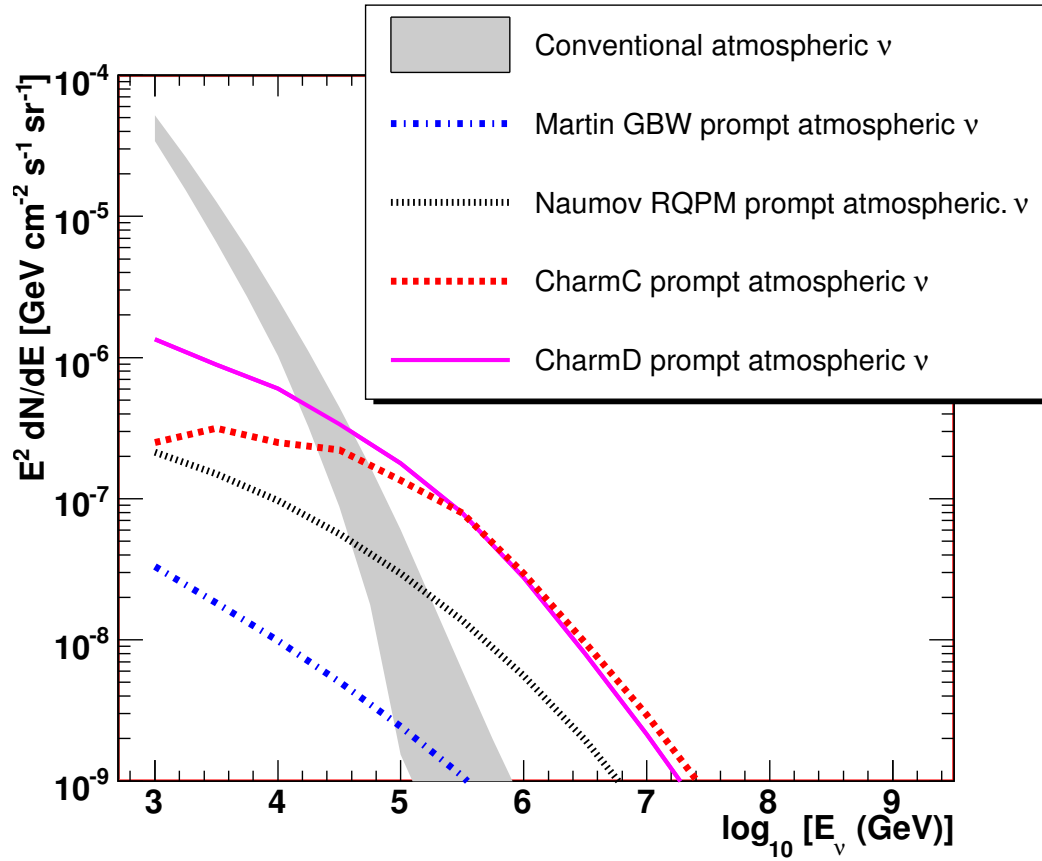


Figure 4.2: Prompt atmospheric neutrinos are predicted to follow a harder spectrum than conventional atmospheric neutrinos. The flux of prompt atmospheric neutrinos is highly uncertain and predictions range over several orders of magnitude.

The **Naumov RQPM** (Recombination Quark Parton Model) [35, 36] incorporates intrinsic charm into the calculation of the prompt atmospheric fluxes. Intrinsic charm assumes that there are charm quark/anti-quark pairs in the incoming particle [37]. For instance, a proton is usually thought of as having three components - two up quarks and one down quark (uud). Assuming intrinsic charm means that charm quarks have non-negligible contributions to the proton wave functions. Instead of defining a proton as (uud), it is defined as (uuc \bar{c} d). The charm quarks and anti-quarks arise from gluon-gluon fusion. When particle collisions occur, the quarks recombine into new groupings, hence forming new particles, possibly with charm ($D^+ = c\bar{d}$, $D^0 = c\bar{u}$, $\lambda_c^+ = udc$, ...).

For the Naumov RQPM model, the Z-moment is energy dependent [37].

$$Z_{Ni}(\gamma) = Z_\gamma \left(\frac{E_N}{E_\gamma} \right)^\xi \quad (4.11)$$

where ξ , E_γ and Z_γ are constants directly dependent on the primary cosmic ray spectral index, γ .

Zas, Halzen and Vazquez [33] suggested five different models of the prompt neutrino flux. Each one has a different parameterization of the energy dependence of the charm production cross section. Only two of the models are tested in this analysis, Charm C and Charm D.

The **Charm C** model assumes an energy dependence for the charm cross section that is fitted to experimental data [38] with a $\log^2(s)$ fit. (\sqrt{s} is the center of mass energy of the particle) **Charm D** uses the charm cross section from Volkova [39].

4.3 Existing Prompt Neutrino Upper Limit

The predecessor of this analysis was a 1997 AMANDA-B10 analysis that put an upper limit on the Charm D flux from Zas *et al.*. The upper limit was $4.8 \cdot \Phi_{\text{CharmD}}$. When the published limit is compared to the atmospheric neutrino spectrum, the Charm D flux upper limit crosses over the atmospheric neutrinos between 3 – 30 TeV. Thus, the true prompt flux is expected to begin dominating over the conventional atmospheric neutrino flux at an energy greater than a 3 – 30 TeV, although the most currently accepted models suggest a much high region for the crossover (50 TeV - 1 PeV).

Chapter 5

Neutrino Detection with AMANDA

AMANDA, or Antarctic Muon and Neutrino Detector Array, is an ice-Cherenkov detector located at the South Pole. A team of collaborating scientists from around the world designed and built the detector during the 1990s. Since AMANDA analyses are searching for a small astrophysical neutrino signal among a large background, the search methods have been developed to maximize the signal retention and background rejection.

5.1 Search Method

This analysis uses the Earth as a filter to search for upgoing astrophysical neutrino-induced events. The background for the analysis consists of atmospheric muons and neutrinos created when cosmic rays interact with Earth's atmosphere. The majority of the events registered in the detector are atmospheric muons traveling downward through the ice.

Conventional atmospheric neutrinos arise from the decay of pions and kaons created in cosmic ray interactions with the atmosphere. Atmospheric neutrinos are able to travel undisturbed through the Earth. They can be separated from atmo-

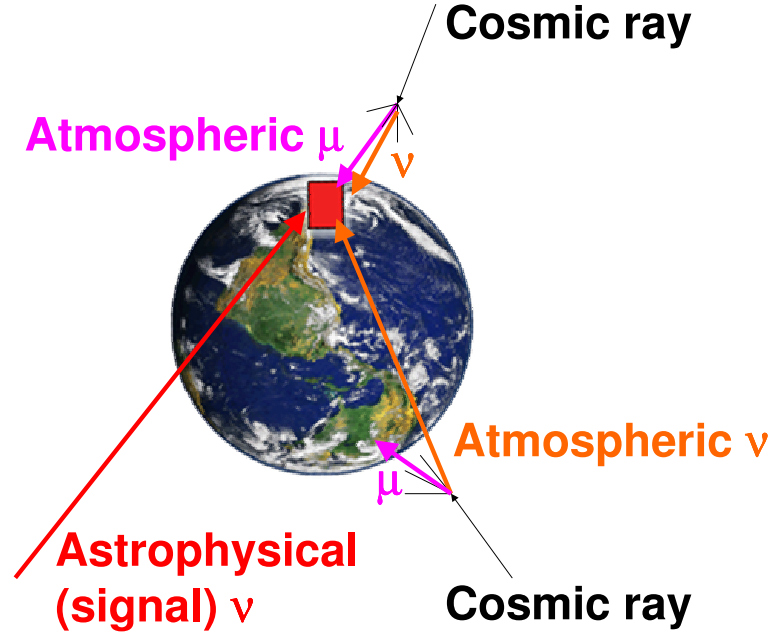


Figure 5.1: Types of events in the detector.

spheric muons by their direction, namely by demanding that the reconstructed track is upgoing. The conventional atmospheric neutrino flux asymptotically approaches a $\Phi \sim E^{-3.7}$ spectrum in the multi-TeV range.

In the initial sample of 5.2×10^9 events, many downgoing events were misreconstructed as upgoing tracks. Misreconstruction happens because photons scatter in the ice, causing directional and timing information to be lost. Hence, the selected upgoing event sample not only contains truly upgoing neutrinos, but a certain fraction of downgoing atmospheric muons.

An energy-correlated observable was used to separate neutrino-induced events since the predicted astrophysical neutrino flux has a much harder energy spectrum ($\Phi \propto E^{-2}$) than the conventional atmospheric neutrinos from pions and kaons. Any excess of events at high energy over the expected atmospheric neutrino background

indicates the presence of a signal.

The search method can be summarized with the following three steps.

1. Use the zenith angle from the reconstructed track to reject obviously downgoing events.
2. Select events that have observables more consistent with typical long upgoing tracks. This separates truly upgoing events from misreconstructed downgoing events.
3. Use an energy-related observable (number of OMs triggered) to separate upgoing atmospheric neutrinos from upgoing astrophysical neutrinos.

5.2 AMANDA Detection Principle

Since neutrinos have no charge and are hence hard to detect, they are studied indirectly by the Cherenkov light that they induce. Cherenkov light occurs when a charged particle travels faster than the speed of light in a transparent medium. Light travels slower in media other than a vacuum and the speed of light is adjusted by a refractive index, n .

$$c_{medium} = \frac{c_{vacuum}}{n} \quad (5.1)$$

The particle travels faster than the light can propagate away from it and hence the light lags behind in a wavefront with a fixed angle [1]. The critical angle formed by the Cherenkov cone obeys the equation:

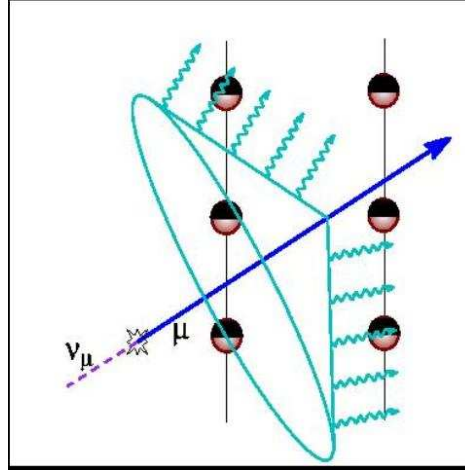


Figure 5.2: A muon neutrino and the Cherenkov cone.

$$\cos\theta = \frac{1}{n\beta} \quad (5.2)$$

where $\beta = v/c$ and v is the particle velocity. In ice, $n=1.32$ and the Cherenkov angle is $\sim 41^\circ$ for relativistic particles ($v \sim c$).

When a neutrino interacts with matter, charged particles are created. If a neutrino-matter interaction occurs in water or ice, then the resulting particles emit Cherenkov light that can be detected by photosensors. If many sensors are distributed throughout a three-dimensional volume of water or ice, then the position and timing information available for each detected photon can be used to reconstruct the path of the charged particle. A neutrino-induced muon travels in the same direction as the neutrino with a median space angle difference of [5]

$$\frac{0.7^\circ}{(E_\nu/\text{TeV})^{0.7}} \quad (5.3)$$

As charged particles such as muons travel through matter, they lose energy. There are two types of energy loss in matter, continuous and stochastic. Ionization of

the ice through which a muon travels leads to a continuous loss of $\sim 2MeV/(g/cm^2)$ (roughly independent of energy, although it rises slightly above 1 GeV). Stochastic losses occur from bremsstrahlung, electromagnetic interactions with nuclei and e^+e^- pair production [3] and lead to losses proportional to the energy. The energy loss rate for muons in matter is:

$$\frac{dE}{dX} = -\alpha - E/\xi \quad (5.4)$$

where α represents continuous losses and ξ is a factor that combines the effects of bremsstrahlung, hadronic interactions and pair production. At the critical energy, ϵ , continuous and discrete losses are equally important. After traveling through matter to a depth of X , a particle with an initial energy E_0 has energy

$$\langle E(X) \rangle = (E_0 + \epsilon)e^{-X/\xi} - \epsilon \quad (5.5)$$

Because of muon energy losses, atmospheric muons can not travel to the detector from the far side of the Earth. However, neutrinos can. The prediction that neutrinos could be observed with Cherenkov radiation in a large transparent medium led to the idea of water/ice Cherenkov detectors in the 1960s.

5.3 AMANDA Detector

The AMANDA detector is comprised of 677 photomultiplier tubes installed upside-down in glass spheres, attached to large cables and lowered into deep holes in the polar ice cap.

Each AMANDA string was deployed after drilling through the polar ice with a

hot water drill. As the main cable was lowered into each hole, optical modules (OMs) were attached at regular spacings. An OM consists of a glass pressure vessel that surrounds an 8-in photomultiplier tube (PMT) and the electronics used to operate it. Each OM is connected to the main cable and information from each OM is transmitted up to the surface when photons are detected. The OMs are located at depths between 1500 m and 2000 m below the Antarctic surface.

The detector was called AMANDA-B10 when only 10 strings were deployed. The strings were layed out so that the instrumented ice volume was cylindrical. In this configuration, AMANDA took data from 1997-2000. In 2000, an outer ring of strings was added and AMANDA-II began operation with 19 strings. Each string was connected on the surface to a computer system in MAPO, a building at the South Pole. An event is recorded in the detector every time at least 24 OMs report seeing a photon within a $2.5 \mu\text{s}$ window.

AMANDA is operated in conjunction with SPASE, the South Pole Air Shower Experiment. SPASE consists of 30 surface tanks that are used to measure downgoing air showers caused by cosmic ray interactions in the atmosphere. As discussed in later sections, downgoing atmospheric muons are a calibration source for the detector.

The AMANDA collaboration grew to include members from about 20 collaborating institutions. After years of successful operation, AMANDA merged with the IceCube collaboration in order to build a much larger, cubic kilometer detector. AMANDA is now considered the inner core detector of IceCube. The IceCube strings surround AMANDA and the digital optical modules (DOMs) lie between 1450 and 2450 meters. IceCube will eventually contain 80 strings and instrument one cubic

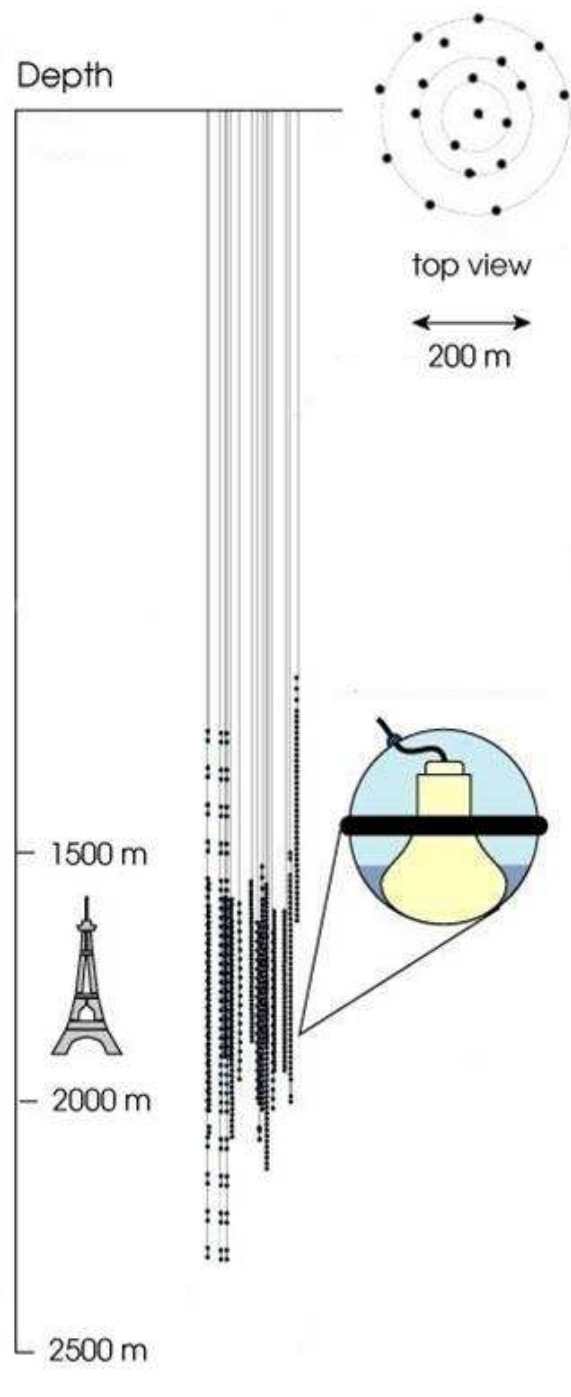


Figure 5.3: Layout of the AMANDA detector.



Figure 5.4: Optical Module.

kilometer of ice. Currently, 22 IceCube strings have been deployed and each contains 60 DOMs spaced by 17 meters. The IceCube string layout forms a hexagonal structure, with each string separated by 125 meters.

5.3.1 AMANDA Coordinate System

AMANDA aims to separate atmospheric muons from neutrino-induced muons by their directional information. Since the desired neutrino signal can travel all the way through the Earth, it is natural to design the detector to best identify this type of event. Hence, the PMTs face downward.

An event which travels from the South Pole surface directly downward into the ice has a zenith angle of 0° . An event which travels from the far side of the Earth is considered upgoing. Exactly upgoing events have a zenith angle of 180° .

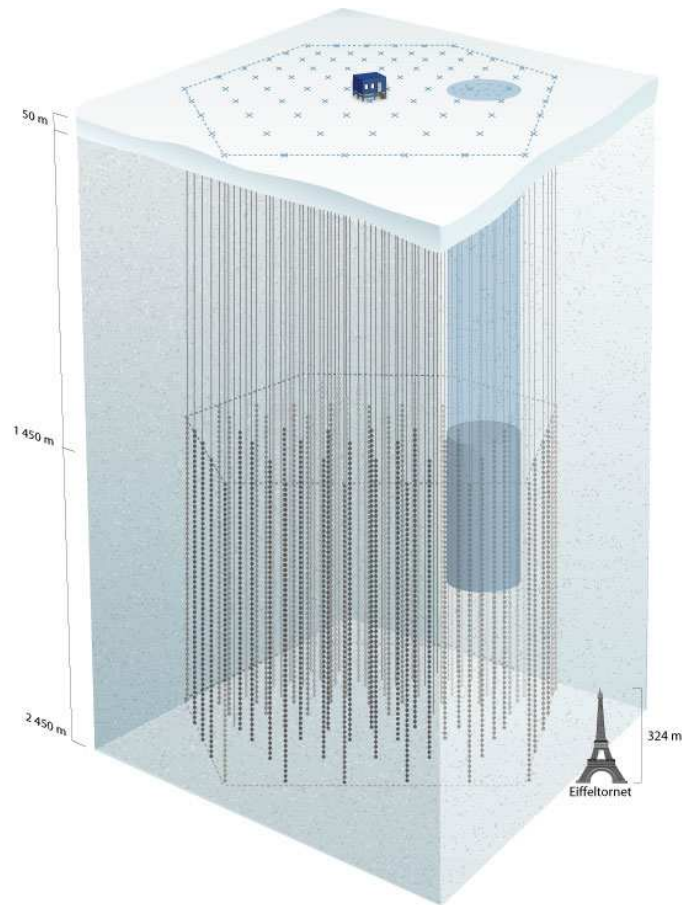


Figure 5.5: When the IceCube detector is complete, it will contain 80 strings and cover one cubic kilometer of ice. The AMANDA detector lies within the IceCube array and is represented by the cylinder in the figure.

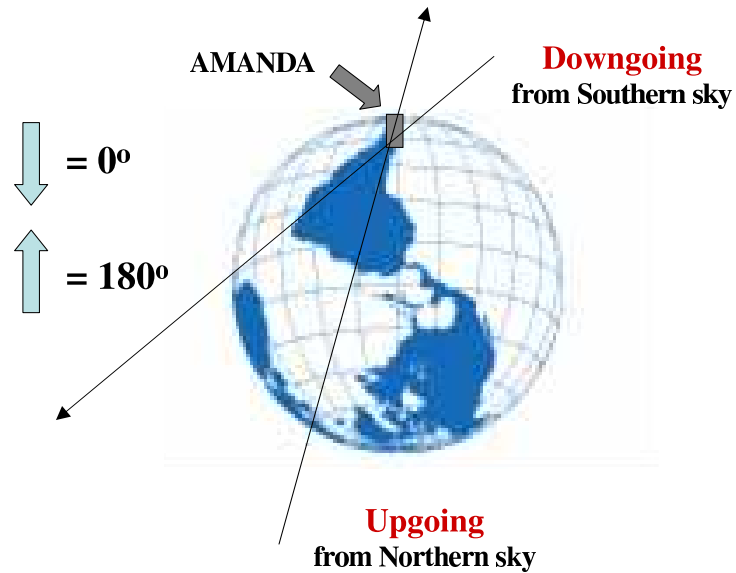


Figure 5.6: AMANDA coordinate system

5.4 Optical Properties of South Pole Glacial Ice

Unfortunately, photons emitted in the ice do not necessarily travel in straight lines. Due to properties of the ice, the photons may be absorbed or may scatter before being detected by an OM. Scattering and absorption in the ice delay the photon arrival times. This leads to larger values of the space angle difference between the true and reconstructed track of the particle.

Photons scatter more in dirty (dust-filled) or bubble-laden ice. At shallow depths, the ice contains many bubbles. Hence, AMANDA-II was built deeper than this region in order to alleviate scattering difficulties. Layers of dust in the relatively pure, deep polar ice reveal different periods of climatological change [40].

In order to model the Cherenkov cone correctly, it is necessary to simulate the clean and dirty layers of the ice. Lasers installed with the OMs are used to measure the scattering and absorptivity of the ice at different depths.

The geometric scattering length, λ_s , is the average distance traveled by a particle between successive scatters [40]. After one scatter, the average change in the particle's direction is $\langle \cos \theta \rangle$. After being scattered n times, the photon has direction $\langle \cos \theta \rangle^n$. In this situation where a high energy photon is scattering off dust particles in the ice, the scattering is mostly forward and hence anisotropic. The effective scattering length, λ_e , is used because of the anisotropy. After each scatter i , the photon has moved a distance $\lambda_s \langle \cos \theta \rangle^i$. Assuming a large number of scatters, n , leads to the following relation:

$$\lambda_e = \lambda_s \sum_{i=0}^n \langle \cos \theta \rangle^i = \frac{\lambda_s}{1 - \langle \cos \theta \rangle}. \quad (5.6)$$

The effective scattering coefficient is the reciprocal of the effective scattering length:

$$b_e = \frac{1}{\lambda_e}. \quad (5.7)$$

The effective scattering is depth and wavelength dependent and is shown in Figure 5.7. The power law fit with AMANDA data indicates that the wavelength dependence of b_e can be described by $b_e(\lambda) \propto \lambda^{-\alpha}$, where $\alpha = 0.9 \pm 0.03$ [40].

The absorption length, λ_a , characterizes the distance at which the survival probability is $1/e$. The absorption coefficient, a , is the reciprocal of λ_a :

$$a = \frac{1}{\lambda_a} \quad (5.8)$$

A two-component absorption model was used [40] to characterize the absorption coefficient as a function of depth, z .

$$a(z) = C_{dust}(z)\lambda^{-\kappa} + A_{IR}e^{-\lambda_0/\lambda} \quad (5.9)$$

C_{dust} is the dust concentration factor which varies as function of depth. The values of the constants were determined to be $A_{IR} = (6954 \pm 973)\text{m}^{-1}$ and $\lambda_0 = (6618 \pm 71)\text{ nm}$. A fit to AMANDA data indicates that $\kappa = 1.08 \pm 0.01$. The absorption coefficient as a function of depth and wavelength is shown in Figure 5.7.

The results of the extensive AMANDA analyses of the optical properties of the ice have been incorporated into the ice models used in this analysis. Three dirty layers of ice were found at AMANDA depths and were included in the simulation. This analysis uses ice simulated with the Muon Absorption Model, MAM. Although the dust layers are simulated, optical properties of the ice remain one of the largest systematic uncertainties in the detector.

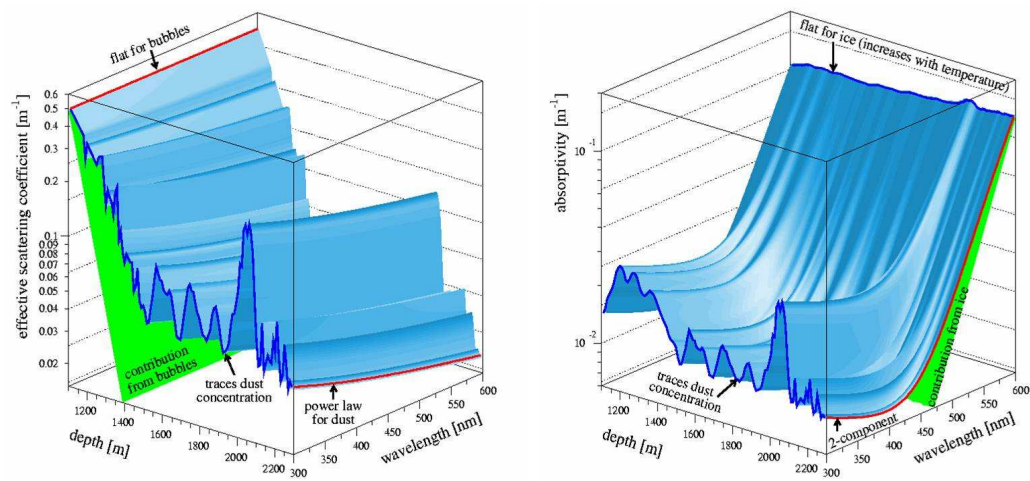


Figure 5.7: The scattering (left) and absorption (right) properties of light vary as a function of depth and wavelength in the polar ice.

Chapter 6

Preparation of the 2000 - 2003 Sample

6.1 Livetime and Triggers

An event triggers the detector when 24 or more optical modules are hit within $2.5 \mu\text{s}$. During the four-year span from 2000 to 2003, 7.14 billion events were recorded by AMANDA-II.

	2000	2001	2002	2003
Number of Triggers	1.37×10^9	2.00×10^9	1.91×10^9	1.86×10^9

The detector is not always running or accepting data, hence the livetime is 807 days rather than the four years spanned by the data files. Detector deadtime occurs for a fraction of a second while an event is being recorded. Upgrades and maintenance during the South Pole summer months also reduce the livetime. The adjusted livetime is listed below for each year. The first and last days of acceptable data for the year are listed in the final two columns. Due to different instrument settings and the behavior of the detector, the year 2000 is best characterized by three separate periods.

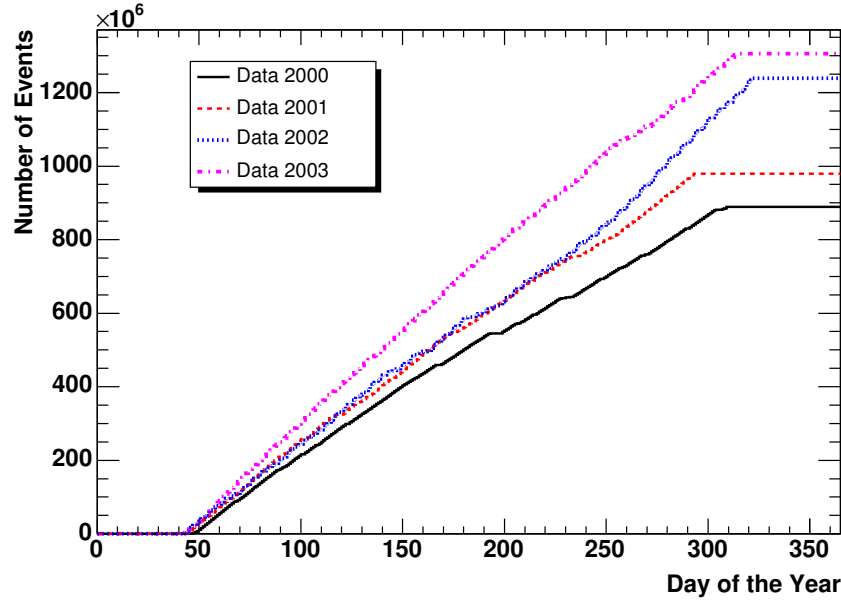


Figure 6.1: Cumulative number of events.

Year/Period	Detector Livetime (<i>days</i>)	First Day	Last Day
2000p1	58.9	47	125
2000p2	86.5	126	244
2000p3	51.6	245	309
2001	193	44	293
2002	204	43	323
2003	213	43	315

Searching for an astrophysical neutrino signal among 7.14 billion events could be likened to searching for a needle in a haystack. As already mentioned, the detector is dominated by events triggered by downgoing muons created from cosmic ray interactions with the atmosphere. The first step in reducing the data to a more manageable size is to remove all events that appear to have traveled downward through the detector. Unfortunately, first-guess techniques for the event direction are not enough to reject all downgoing backgrounds, as many events may be misreconstructed. As the data volume is reduced, more accurate, but computer-intensive reconstruction

techniques can be applied to the remaining events.

The filtering process includes reconstructing the track direction of each event and then removing any events that appear to be background. The filtering process occurred in five stages and is summarized in Table 6.2. The following sections explain the filtering techniques applied.

6.2 Rejection of Atmospheric Muon Background

At Filtering Stage 1, a first-guess reconstruction was applied to every data event. The procedure, known as a direct walk reconstruction, considered a straight line track between every pair of triggered optical modules [42]. A track between two hits was only labelled as a candidate if the two hits occurred within 30 ns of the time it would take for light to travel between the two optical modules. If multiple candidates existed, the selected track was the one with the most neighboring candidates within a space angle difference of 15° . Figure 6.2 shows the zenith angle of the reconstructed tracks for all events at the beginning of the analysis. Vertically downgoing tracks have a reconstructed zenith angle θ of 0° ($\cos(\theta)=1$).

After using the direct walk reconstruction to infer the incoming zenith angle of every event, all events reconstructed with zenith angles less than 70° were removed. To improve the background rejection, another reconstruction method, JAMS, was then applied.

The JAMS reconstruction uses a pattern matching algorithm when fitting a track to the data [43]. JAMS is particularly designed to eliminate coincident downgoing atmospheric muons in the detector since they can be misreconstructed as a single upgoing event. When JAMS is applied, 50 different input directions are searched for

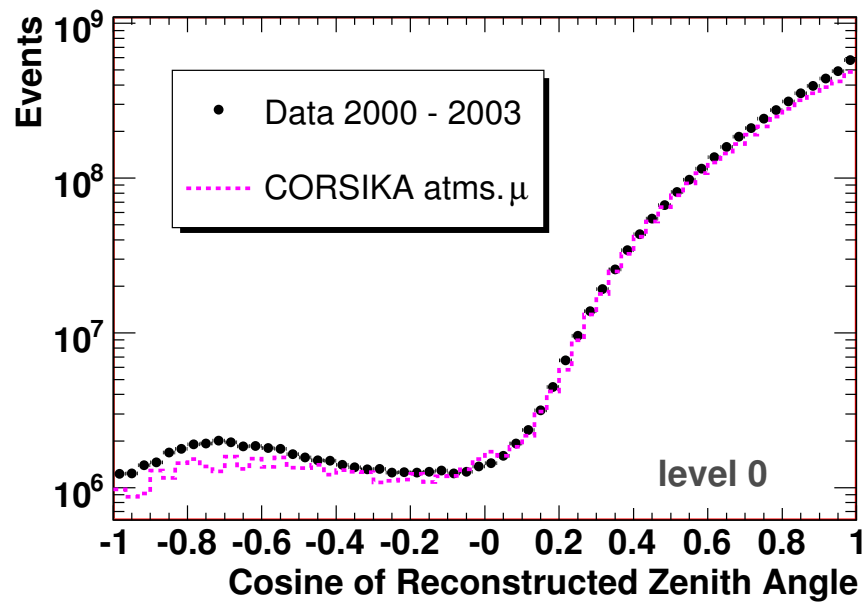


Figure 6.2: The cosine of the reconstructed zenith angle is shown for every event at the beginning of the analysis. The experimental data is dominated by downgoing atmospheric muons. Events reconstructed as upgoing appear on the left side of the plot and downgoing events appear on the right.

clusters of events. A cluster has at least 7 close, on-time hits for the suggested track. A simplified Gaussian likelihood is then maximized to get the track parameters for each of the identified clusters. A neural net trained to separate good and bad reconstructions is used to rank each of the clusters. The track from the highest ranking cluster is the JAMS track. If the JAMS reconstruction indicated that the zenith angle of the track was less than 80° , the event was removed.

6.3 Reconstruction Methods

Track parameters were adjusted to maximize the log likelihood, given the observed light pattern [42]. Many of the Cherenkov photons scatter multiple times as they travel through the ice and this changes their direction and delays the times at which they are likely to be detected. For a given photon observation and proposed track, a probability can be calculated that suggests how likely it is that a particular hit was caused by that track. We denoted this the probability density function or p.d.f., $p(x_i|\vec{a})$, where x_i describes a particular hit and \vec{a} describes the parameters of the track. The likelihood of a track is the product of the values of the p.d.f. for the observed photon arrival times.

$$\mathcal{L}(x|\vec{a}) = \prod_i p(x_i|\vec{a})$$

The Pandel function was developed to describe the arrival times of light from the Cherenkov cone for the Baikal experiment [44]. This function describes propagation of light in media with both diffusion and absorption effects. As the light travels, it scatters instead of taking a direct path to the optical modules. Simulation samples

	2000	2001	2002	2003
Number of Triggers	1.37×10^9	2.00×10^9	1.91×10^9	1.86×10^9
Filtering Stage 1	4.54×10^7	8.18×10^7	6.83×10^7	6.53×10^7
Filtering Stage 2	5.50×10^6	6.87×10^6	7.59×10^6	8.02×10^6
Filtering Stage 3	1.63×10^6	1.90×10^6	2.10×10^6	2.22×10^6

Table 6.1: The total number of data events at each filtering stage.

were used to fit the parameters of the function for the AMANDA detector and its local ice [42]. The function was then modified to account for PMT time jitter. The Pandel function is used to parameterize the p.d.f.

Because the initial track hypothesis is not always optimal, an iterative technique was used in which each event was reconstructed 32 times using the Pandel parameterization. Each iteration of the track reconstruction shifts the zenith and azimuth of the track and moves it to pass through the center of gravity of the hits. The best track resulting from an iterative reconstruction maximizes the log likelihood of the observation. Hence, in the Pandel reconstruction, the log likelihood of the Pandel p.d.f. is maximized.

Because iterative reconstructions require more computing time, they were not used until the Stage 1 filtering removed the obviously downgoing events from the data set. The 32-iteration Pandel reconstruction was considered the most accurate reconstruction performed on this data. At Filtering Stage 3, all events with Pandel-reconstructed zenith angles less than 80° were removed.

6.4 Techniques to Further Improve Background Rejection

Several other techniques were used to improve background rejection. The first technique described here is an additional 64-iteration reconstruction. This zenith-weighted (Bayesian) reconstruction provided valuable information for removing background later in the analysis. Methods were also employed to remove electronic crosstalk and other fake events. In the final filtering stages, two other reconstructions were performed and their outputs used to characterize the events.

6.4.1 Zenith-weighted (Bayesian) Reconstruction

The zenith-weighted reconstruction uses our prior knowledge about the atmospheric muon flux to perform each track reconstruction [42]. Based on previous measurements with AMANDA, it is known that most of the events that trigger the detector are atmospheric muons. Even without knowing any information about an event, it is much more likely that the event actually traveled downward through the detector rather than upward. Hence, a weighting function was derived based on the atmospheric muon zenith angle distribution. If, for instance, an upgoing and downgoing track are being considered as possible fits for a given event, the downgoing track would be given a much larger weight and would be the preferred reconstructed track direction.

The zenith-weighted reconstruction is based on Bayes' theorem. Bayes' theorem defines the probability of a situation A occurring given that situation B is true. The theorem states that

$$P(A|B) = \frac{P(B|A)P(A)}{P(B)}. \quad (6.1)$$

In order to use this theorem, one must have prior knowledge of the situation.

In other words, one must know $P(B|A)$ (the probability of B occurring if A is true), $P(A)$ (probability of A occurring) and $P(B)$ (probability of B occurring).

In this scenario, $P(B|A)$ corresponds to the probability that the reconstructed track (assumed to be true) produces the observed events. This is the likelihood described earlier. $P(A)$ is the prior probability of observing a track in the direction indicated by the reconstruction. Since it is known that atmospheric muons traveling downward through the detector make up most of the background (downgoing atmospheric muons:upgoing atmospheric neutrinos = $10^5:1$), there is a very strong chance that the true track of the particle was downgoing. A weighting function was derived based on the zenith distribution of downgoing atmospheric muons and this represents $P(A)$. $P(B)$ is a normalization factor for the probability function.

When the zenith-weighted reconstruction is performed, the maximized quantity is the p.d.f., $P(B|A)$, times the prior function, $P(A)$. The assumed prior weights the function so that the resulting tracks are downgoing. Hence, truly upgoing events have low likelihood values for this reconstruction.

6.4.2 Removal of Electronic Crosstalk

Electrical crosstalk between channels causes fake hits to register in the detector [45]. AMANDA strings 5 - 10 are twisted pair cables which means that several cables are wound together in the ice. When an electrical signal is generated by an optical module, the signal travels up the cable to the counting house. Sometimes, the signals leak off into neighboring cables that are twisted into the same string bundle. This can induce hits in optical modules attached to other cables, but located in the same ice hole. Crosstalk is characterized and removed in two ways during filtering.

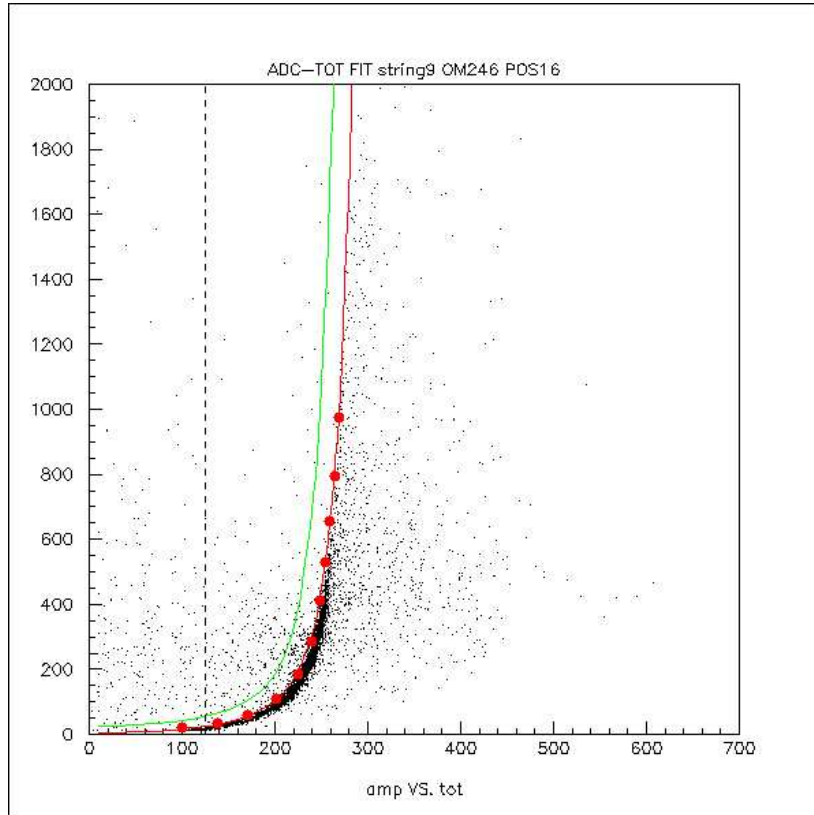


Figure 6.3: Time-over-threshold for the observed light pulse is on the x-axis while amplitude is on the y-axis. Fake hits caused by crosstalk appear in the lower left corner, at small values of the amplitude and the time-over-threshold.

First, crosstalk events can be identified by their pulse shape signatures. Crosstalk hits are very narrow signals and hence they show unnaturally short time-over-threshold values. When examining a two-dimensional plot of ADC (amplitude of light detected) vs. time over threshold, crosstalk hits cluster in the low amplitude, short time-over-threshold corner.

Crosstalk can also be identified by the pattern of fake hits induced. Some optical modules are known as *talkers* because they tend to induce fake hits preferentially in

other *receiver* modules. Measurements were done in which a diffuser ball was flashed near an optical module. All other optical modules were tuned to high threshold conditions, essentially turning them off. In an ideal situation, only the optical module hit by the diffuser ball light would register a signal. However, hits on other optical modules were recorded, hence indicating that crosstalk occurred.

A map was created that indicated which optical modules were most likely to induce crosstalk in others. During crosstalk cleaning, hits were removed if a correlation was seen between hits and the talker-receiver map. Hits were also removed if they fell in the low amplitude, short time-over-threshold region described above.

6.4.3 Removal of Non-Photon Events

As described in the crosstalk section, not all hits that appear in the detector are real. Flare events represent another class of fake events. Flare events are dominated by hits that are not induced by photons triggering the optical modules. It is not known what causes these non-photon hits.

Flare checking is a procedure intended to remove events that have too many non-photon hits [46]. Nine indicators were defined and established to quantify the number of non-photon hits in an event. Unfortunately, some good events also contain non-photon hits. The problem is to separate *good* events from *flare* events based on the number of non-photon hits. Using the nine indicators, events were removed if they contained too many non-photon hits.

The nine flare indicators were developed based on strange behavior seen in some event observables [46]. Non-photon events can be identified because they do not show typical pulse lengths. They can be either too long or too short. The beginning or end

of the pulse may not be observed because it occurred outside of the trigger window. This is called a missing edge. A number of optical modules are listed as dead and hits in these channels indicate flary events. Also, an event is most likely flary if there are many hits on the twisted pair channels but very few hits along other types of strings.

Events were removed if they had more than 10 hits attributed to the following three indicators:

1. number of hits that were too short on the twisted pair strings
2. number of hits in strings 1-4 of AMANDA-B10 relative to the number of hits in string 5-10
3. the relative number of hits on strings 5-10 versus strings 11 - 19.

6.4.4 Paraboloid Reconstruction

A paraboloid fit was performed on each event. $\mathcal{L}(\mathbf{r}, z, a; P)$ is the likelihood for a track direction with point \mathbf{r} along the track, zenith z , azimuth a and pattern of hits, P . $\mathcal{L}_{\text{best}}$ is the likelihood associated with the best reconstructed track for the event (in this case, the 32-iteration Pandel track). The parameter space is searched in zenith and azimuth until:

$$\Delta(-\log\mathcal{L}) = (-\log\mathcal{L}_{\text{ellipse}}) - (-\log\mathcal{L}_{\text{best}}) = 0.5 \quad (6.2)$$

A confidence ellipse is drawn in space about the zenith and azimuth coordinates of the track. The ellipse covers 1σ in either coordinate, hence having a probability of 39.4% of containing the true track direction. The median of this distribution

represents a 50% probability that the ellipse contains the true track direction. The width of the ellipse corresponds to the uncertainty in the track parameters. When expanded to three dimensions, the likelihood space is fitted to a paraboloid and a minimization is performed to determine the paraboloid track. The range covered by the confidence paraboloid in each parameter is known as the paraboloid error. The size of the paraboloid errors is used later in the analysis to estimate the angular resolution of each event.

6.4.5 Velocity of Line Fit

A line fit was added in the final step of filtering. The fit constructs a track assuming that the muon travels a straight path with some velocity, v . It does not take the Cherenkov cone or the optical properties of the ice into account [42]. The absolute speed of the fit can be used to classify events in the detector. Long muon tracks have larger speeds than cascades.

6.5 Event Simulation

This analysis relied on simulated data sets of background and signal events. Sixty-three days of downgoing atmospheric muons were simulated with CORSIKA [41] version 6.030 and the QGSJET01 hadronic interaction model. The events were simulated with a $\Phi \propto E^{-2.7}$ primary energy spectrum. These downgoing events are so frequent (~ 80 Hz at trigger level) that two atmospheric muon events produced by unrelated primaries often occur in the detector during the same detector trigger window of $2.5 \mu\text{s}$. These coincident muon events may be caused by two muons which are each individually incapable of triggering the detector with at least 24 OM hits.

	Cut Applied	Fit Number
Filtering Stage 1		
Hit and OM Cleaning		
Low ToT / amplitude filter		
Direct Walk fit		0
	Zenith (direct walk) $> 70^\circ$	
Direct WIMP fit		1
CFirst (cascade) fit		2
Pandel (16-iter.)		3
Cascade SPE		4
Cascade MPE		5
JAMS		6
Filtering Stage 2		
	Zenith(JAMS) $> 80^\circ$	
Crosstalk Cleaning		
Pandel (32-iter., JAMS seed)		7
MPE (16-iter., Pandel seed)		8
Bayesian (16-iter, Pandel seed)		9
Filtering Stage 3		
	Zenith(Pandel 32-iter.) $> 80^\circ$	
Smoothness calculation		
Cascade likelihood (16-iter.)		10
Paraboloid		11
Filtering Stage 4		
Bayesian (64-iter., Pandel seed)		12
FlareChecker		
	Flrshrtm+Flrndcb1+Flrndc11 < 10	
Filtering Stage 5		
Line Fit		13

Table 6.2: The atmospheric muon background was reduced by three orders of magnitude by a series of filtering requirements.

However, their combined hits trigger an event and the timing patterns of the light from the two tracks may be such that the reconstruction results in a single upgoing track. These coincident muon events were simulated for 826 days of livetime and have a frequency of about $\sim 2\text{-}3$ Hz at trigger level.

Muon neutrinos with a $\Phi \propto E^{-1}$ spectrum were simulated with `nusim` [48] and reweighted to atmospheric neutrino flux predictions [49, 50, 51, 52, 53], as well as an astrophysical muon neutrino flux of $E^2\Phi = 1 \times 10^{-6} \text{ GeV cm}^{-2}\text{s}^{-1}\text{sr}^{-1}$. The normalization of the test signal spectrum, which is irrelevant when setting a limit, was taken to be approximately equal the previous upper limit from the AMANDA-B10 diffuse analysis [24].

6.5.1 Preparation of Simulated Events

Every operating season, the conditions and electronic settings for the detector are slightly different. For this reason, simulated events were generated to mimic the exact conditions of the detector during a given period or year. For instance, a particular optical module may have been acceptable for use in a 2001 analysis, but not in 2003.

Simulation was generated for atmospheric muons and neutrinos, coincident atmospheric muons, and astrophysical neutrinos. The amount of each type of simulation that was generated varied based on available computer resources. It would be too computer intensive to generate one day of simulated livetime for every day of livetime that the detector was actually running during 2000 to 2003. Hence, the simulation represents smaller livetimes than in the actual data. The simulation events were scaled to match the livetime of the data during a particular period or year.

Year / Period	Coincident Muon Simulation Livetime (days)	Atmospheric Muon Simulation Livetime (days)	Detector Livetime (days)
2000 period 1	139.1	9.9	58.9
2000 period 2	136.6	9.9	86.5
2000 period 3	139.4	9.9	51.6
2001	138.3	10.1	193
2002	133.6	12.1	204
2003	139.1	10.9	213

Atmospheric muons and coincident muons are simulated with their supposed energy spectrum, $\Phi \propto E^{-3.7}$. The generation of events with the true energy spectrum makes it very time consuming to accumulate acceptable statistics at high energy. However, `nusim` is generated with a $\Phi \propto E^{-1}$ spectrum. By generating a flat spectrum in cosine of the zenith angle, the `nusim` events can be reweighted to represent atmospheric or astrophysical neutrinos. Hence, the generated `nusim` [48] livetime cannot be listed in the table. Instead, each event receives a weight based on equation 6.3. Not all of these events trigger the detector. Only a fraction survive to the higher filtering levels.

$$\text{nusim weight} = I \times \Phi \times E \times A \times L \times \Omega \times \ln(E_{high}/E_{low}) / (N_{files} \times N_{events}) \quad (6.3)$$

where

I = interaction probability

Φ = flux from model [$\text{GeV}^{-1}\text{cm}^{-2}\text{s}^{-1}\text{sr}^{-1}$]

E = Energy [GeV]

A = Area [cm^2]

L = Livetime [s]

Ω = Solid angle [sr]

$\ln(E_{high}/E_{low})$ = Energy range over which the events were generated

N_{files} = number of files generated

N_{events} = number of events generated per file

Number of Events Generated	2000 period 1 $\times 10^6$	2000 period 2 $\times 10^6$	2000 period 3 $\times 10^6$	2001 $\times 10^6$	2002 $\times 10^6$	2003 $\times 10^6$
ν	1.00	1.00	0.60	2.39	2.52	2.60
$\bar{\nu}$	1.00	1.00	0.60	2.39	2.55	2.59

The simulated events underwent the same reconstruction procedures as the data and had to satisfy the same zenith angle requirements.

After using the filtering levels to require that events must have entered with zenith angles greater than 80° , there would ideally have been no remaining simulated atmospheric muons that truly came from 0° to 80° . However, after Filtering Stage 5, there were 3.6×10^6 simulated downgoing muons remaining. These muons reconstructed with angles between 80° and 180° , despite the fact that they were generated in the opposite hemisphere. These are known as misreconstructed events. The next chapter will describe how these events were removed.

Chapter 7

Obtaining an Upgoing Neutrino Sample

In order to prevent any inadvertent tuning of the event selection criteria that would bias the result, a blindness procedure was followed which required that further event selections were developed only on low energy data and simulation, where the signal is negligible compared to the background. The number of OMs triggered (from now on indicated by N_{ch} , or number of channels hit) is the energy-correlated observable used to separate atmospheric neutrinos from astrophysical ones (Figure 7.1). Only low energy data events (low N_{ch} values) were compared to simulation. High energy data events (high N_{ch} values) were only revealed once the final event selection was established. Energy and N_{ch} are correlated since high energy events release more energy in the detector causing more hits than low energy ones. However, the correlation is not perfect since high energy events occurring far from the detector may trigger only a few OMs.

Event selection was based on observables associated with the reconstructed tracks [42]. In order to separate misreconstructed downgoing events and coincident muons from the atmospheric and astrophysical neutrinos, events were required to have observables consistent with long tracks and many photons with arrival times close to

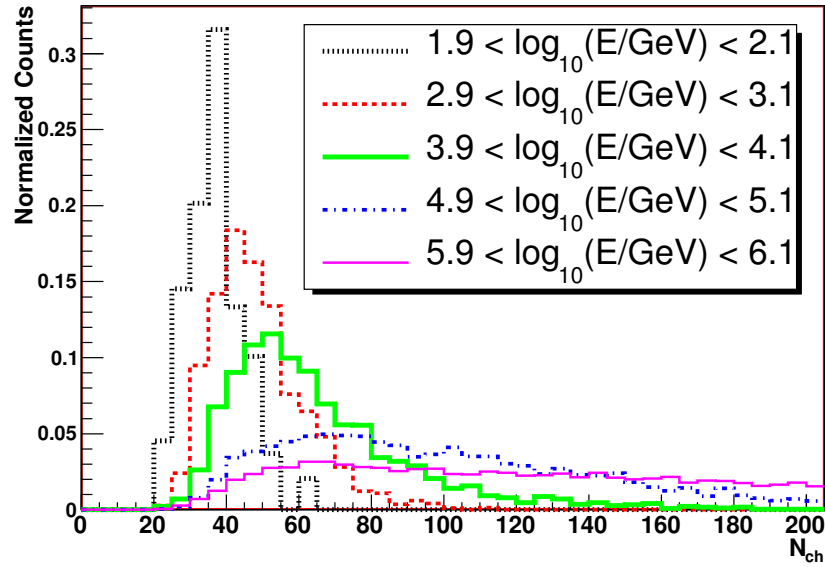


Figure 7.1: The number of OMs hit during an event (N_{ch}) was used as an energy-correlated observable. Each line on this N_{ch} distribution represents events with approximately the same simulated energy. High energy events may not be contained within the detector and hence can trigger a wide N_{ch} span.

those predicted for un-scattered propagation. The number of photons arriving between -15 and $+75$ ns of their expected un-scattered photon arrival time is referred to as the number of direct hits (N_{dir}). The direct length (L_{dir}) is the maximum separation of two direct hits along the reconstructed track. The smoothness (S) is a measurement of how uniformly all hits are distributed along the track and it varies between -1.0 and 1.0 . Positive values of the smoothness indicate more hits at the beginning of a track and negative values indicate more hits occur toward the end. Evenly distributed hits will have smoothness values near 0. The median resolution (MR) is calculated from a paraboloid fit to the likelihood minimum for the track [47]. This method analyzes the angular resolution on an event-by-event basis. Lastly, high quality events have higher values of the logarithm of the up-to-down likelihood ratio, $\Delta L = (-\log \mathcal{L}_{\text{down}}) - (-\log \mathcal{L}_{\text{up}})$. The likelihoods \mathcal{L}_{up} and $\mathcal{L}_{\text{down}}$ are the product of the values of the probability density function for the observed photon arrival times, for the best upgoing and zenith-weighted downgoing track reconstruction [42], respectively. The likelihood ratio requirement was more strict for vertical events than for events near the horizon. Horizontal events tend to have smaller likelihood ratios since the zenith angle difference between the best upgoing and zenith-weighted downgoing track hypothesis is often small.

As seen in Figure 7.2, requiring a minimum value of the track length, for instance, can be a powerful method of rejecting misreconstructed downgoing backgrounds. The event selection requirements for L_{dir} , N_{dir} , smoothness, median resolution and likelihood ratio were established to remove many orders of magnitude more misreconstructed background than upgoing atmospheric neutrinos or signal neutrinos. Events

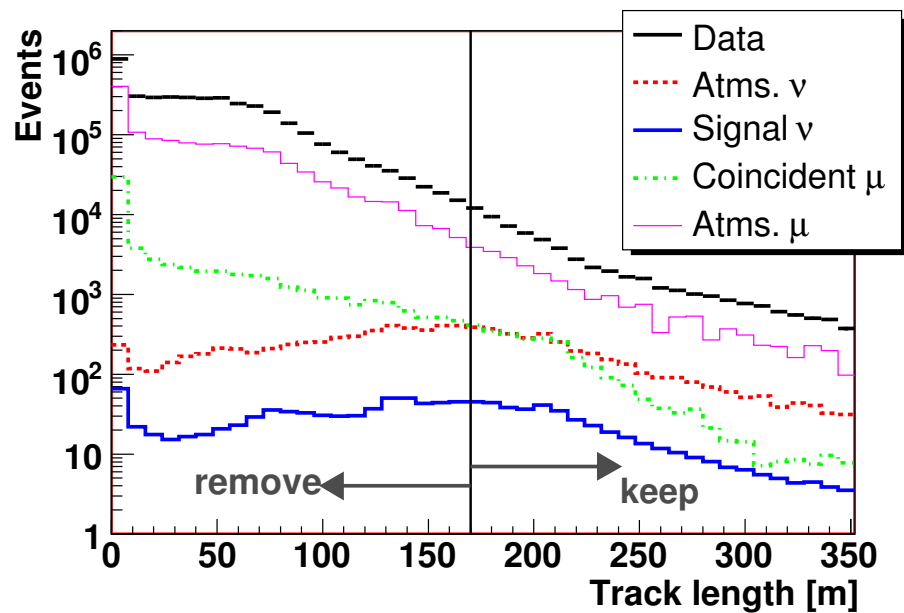


Figure 7.2: The reconstructed track length within the detector is shown. In order to identify muon neutrino tracks, events were required to have long tracks of at least 170 meters. This removed a large fraction of the atmospheric muon simulation, but had a smaller effect on the atmospheric neutrino and signal simulations.

	L0	L1	L2	L3	L4	L5*
Zenith Angle [°]		>80	>80	>80	>80	>100
Number of Direct Hits			>5	>8	>8	>13
Track Length [m]			>100	>130	>130	>170
 Smoothness 				< 0.30	< 0.30	< 0.25
Median Resolution [°]					<4.0	<4.0
Likelihood Ratio (ΔL) vs. Zenith						$\Delta L > -38.2\cos(\text{Zen.}) + 27.506$
Number of Remaining Events	5.2×10^9	7.8×10^6	1.2×10^6	3.5×10^5	1.8×10^5	465

* = level of the final analysis

Table 7.1: The table summarizes the event quality requirements as a function of quality level. Events only remained in the sample if they fulfilled all of the parameter requirements for a given level. The removal of all horizontal events (zenith < 100) contributed to the large decrease in events from L4 to L5.

which did not meet an optimized minimum or maximum value of each parameter were removed.

The event selection requirements were successively tightened, based on the reconstructed track parameters, establishing five quality levels. The requirement is defined for each parameter in Table 7.1. The plots in Figure 7.3 show the zenith angle distribution of all events fulfilling the zenith angle $>80^\circ$ and event observable requirements at the chosen level. Although the entire zenith angle region is being studied, the event selection requirements preferentially retain vertically upgoing events. Horizontal and vertical events must pass the same requirements for track length and number of direct hits, however this is more difficult for horizontal events since the detector is not as wide as it is tall.

After the zenith angle criteria was fulfilled at Level 1, the data mostly con-

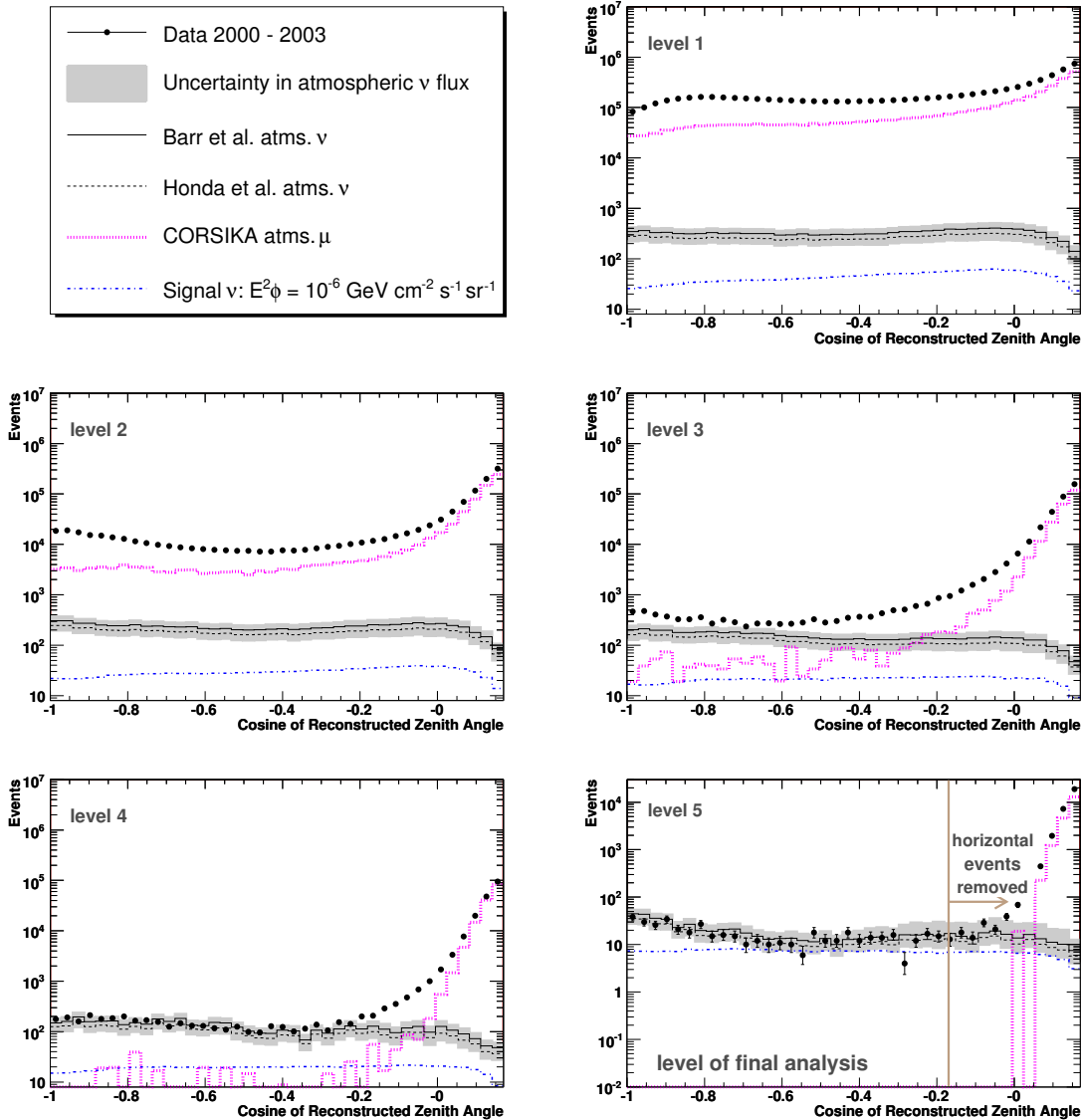


Figure 7.3: The cosine of the zenith angle is plotted for all events surviving the event quality criteria at a given level. Events at $\cos(\text{zenith}) = -1$ are traveling straight up through the detector from the Northern Hemisphere. The initial zenith angle requirement removed events from 0° to 80° (level 1 - top right). Events reconstructed just above the horizon appear at the right side of each plot. Each level represents an increasingly tighter set of quality requirements. As the quality level increased, misreconstructed downgoing muons were eliminated. To ensure a clean upgoing sample, events coming from the horizon were discarded by requiring reconstruction angles greater than 100° . The final analysis was performed at level 5 (bottom right) with horizontal events removed.

tains misreconstructed atmospheric muons (top right, Figure 7.3). As the quality parameters become more restrictive, the data begins to follow the atmospheric neutrino simulation in the upgoing direction and the atmospheric muon simulation in the downgoing direction. At Level 5, the event quality requirements were strong enough to have removed all of the misreconstructed downgoing atmospheric muon events that were simulated. However, just to be sure that the final data set only included atmospheric and astrophysical neutrinos and no misreconstructed downgoing events, an additional zenith angle requirement was imposed. All events were kept if they were reconstructed between 100° and 180° . The analysis continued with the data sample shown at Level 5.

Chapter 8

Separating Atmospheric Neutrinos from Astrophysical Neutrinos

Figure 8.1 shows the N_{ch} distribution for events at Level 5. The optimal place for the energy-correlated event observable requirement was established with the simulation by minimizing the expected Model Rejection Factor (MRF) [54]. The Feldman-Cousins method was used to calculate the median upper limit [55]. The MRF is the median upper limit divided by the number of predicted signal events for the ν_{μ} signal being tested. The MRF was calculated for every possible N_{ch} value and was at its minimum at $N_{\text{ch}} \geq 100$. Hence, the optimal separation of astrophysical and atmospheric neutrinos is achieved with this N_{ch} requirement.

The final event sample was composed of events which pass all event selection requirements (Level 5) and have $N_{\text{ch}} \geq 100$. After the high N_{ch} requirement, the atmospheric neutrino simulation peaked at 10 TeV, while the signal simulation peaked around 100 TeV (Figure 8.2). The energy range defined by the central 90% of the signal with $N_{\text{ch}} \geq 100$ is the energy range for the sensitivity or limit. For this search, the central 90% signal region extends from 16 TeV to 2.5 PeV.

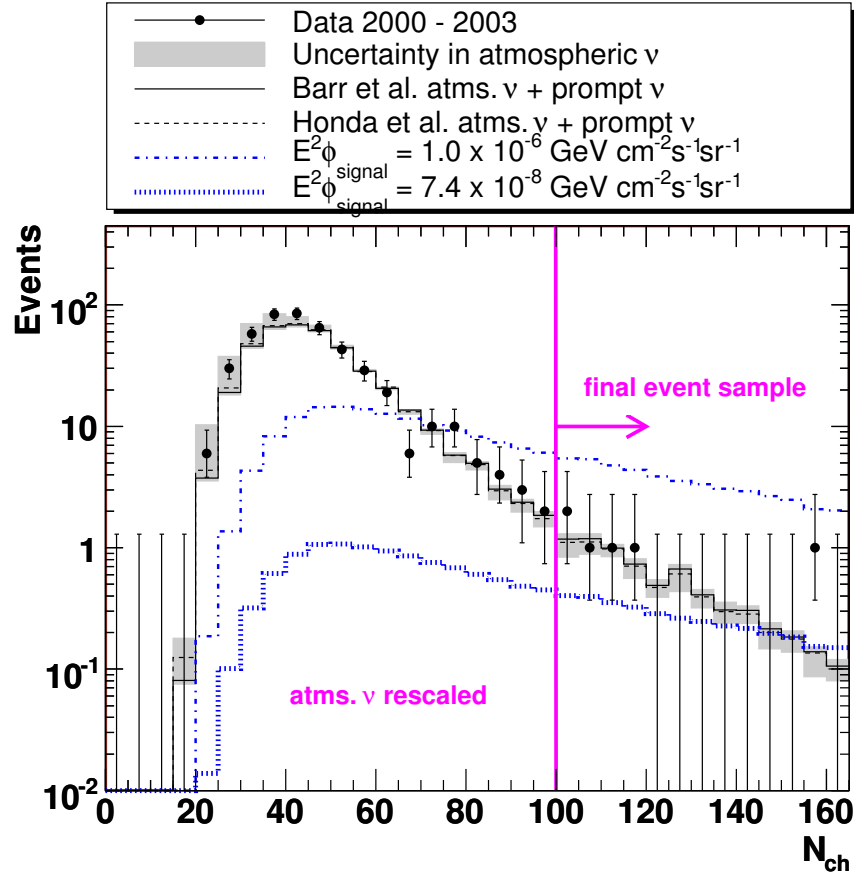


Figure 8.1: N_{ch} , or number of OMs hit. The full data set is revealed. Both conventional and prompt atmospheric neutrinos are shown and their uncertainties are represented by the gray band. The central prompt neutrino flux used here is the average of the Martin GBW [34] and Naumov RQPM [35, 36] models. The signal is rescaled to reflect the new limit.

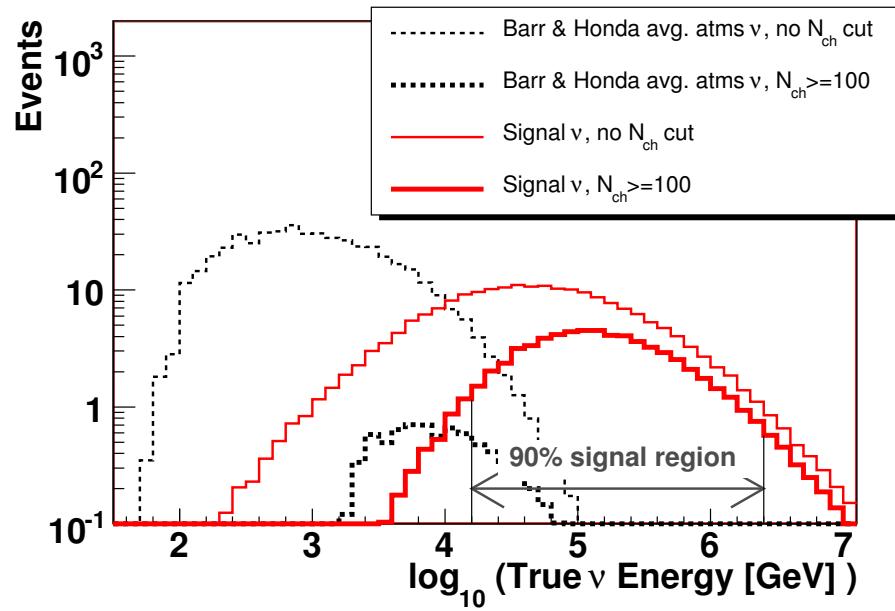


Figure 8.2: The true energy of the simulation is shown for atmospheric neutrino and signal events. The thin dashed (atms. ν) and solid (signal ν) curves represent the number of events before the $N_{\text{ch}} \geq 100$ requirement. The thick dashed and solid lines represent only the events in the high energy sample.

Chapter 9

Effective Area

The efficiency of the detector for neutrinos is quantified by the effective area. In the energy range relevant to this analysis, it increases with energy and is further enhanced by including uncontained events. The effective area is described by the following equation where N represents the number of observed events and T is the detector livetime:

$$\frac{N}{T} = \int A_{\text{eff}}^{\nu}(E_{\nu}, \Omega) \Phi_{\nu} d\Omega dE. \quad (9.1)$$

The effective area as a function of energy is shown for different zenith angle regions in Figure 9.1 (and is tabulated in Tables 9.1 and 9.2). At energies greater than 10^5 GeV, the Earth begins to be opaque to neutrinos depending on direction and the highest energy events are most likely to come from the region around the horizon [56]. In Figure 9.1, the effective area decreases at high energy because tracks with zenith angles between 80° and 100° were discarded. Most of the events that were removed were high energy events from the horizon.

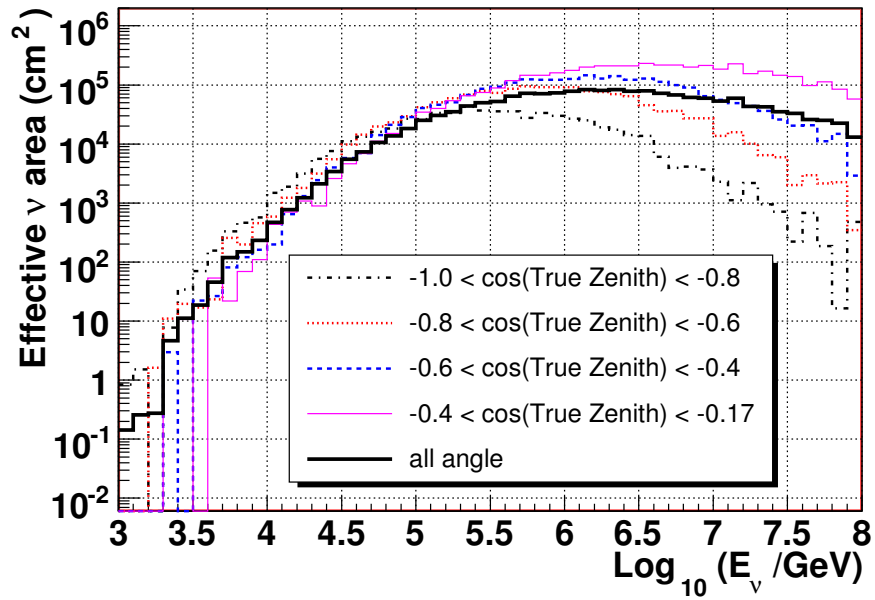


Figure 9.1: Effective area for ν_μ as a function of the true simulated energy in intervals of cosine of the true neutrino zenith angle. The effective area is the equivalent area over which the detector would be 100% efficient for detecting neutrinos. The absorption of neutrinos in the Earth is taken into account. The angle-averaged effective area is represented by the solid black line.

Energy \log_{10} (E/GeV)	$-1 < \cos(\text{Zenith}) < -.8$		$-.8 < \cos(\text{Zenith}) < -.6$	
	ν_{μ} [10^3cm^2]	$\bar{\nu}_{\mu}$ [10^3cm^2]	ν_{μ} [10^3cm^2]	$\bar{\nu}_{\mu}$ [10^3cm^2]
3.6	0.487	0.166	0.279	0.0673
3.8	1.04	1.1	0.652	0.646
4	3.36	2.85	1.82	1.89
4.2	8.74	7.54	4.97	5.56
4.4	18.8	16.2	15.3	12.4
4.6	29.3	30.4	34	26.9
4.8	44.9	46.4	52.7	58.8
5	59.6	65.5	92.6	88
5.2	75.7	69.7	128	121
5.4	72.6	84.4	153	163
5.6	63.5	77.8	180	179
5.8	63.3	66.9	183	188
6	51.9	49.3	170	177
6.2	36.6	39.1	145	151
6.4	27.8	22.6	110	113
6.6	9.97	14.7	72.3	77
6.8	7.8	8.73	54.2	48.2
7	3.39	3.08	29.6	29.5
7.2	3.12	1.44	16.5	15.2
7.4	0.939	0.718	7.97	9.64
7.6	0.864	0.791	5.12	4.15
7.8	0.492	0.521	2.59	2.08

Energy \log_{10} (E/GeV)	$-.6 < \cos(\text{Zenith}) < -.4$		$-.4 < \cos(\text{Zenith}) < -.17$	
	ν_{μ} [10^3cm^2]	$\bar{\nu}_{\mu}$ [10^3cm^2]	ν_{μ} [10^3cm^2]	$\bar{\nu}_{\mu}$ [10^3cm^2]
3.6	0.108	0.0562	0.0752	0.0451
3.8	0.282	0.163	0.178	0.0818
4	0.845	0.93	1.13	0.543
4.2	3.73	3.39	1.98	1.66
4.4	9.74	8.22	7.23	6.02
4.6	21.1	19.9	17.9	18.2
4.8	49.7	43.3	33.2	36.9
5	86.2	77.5	74.2	68.3
5.2	118	119	119	113
5.4	179	165	163	167
5.6	232	217	264	230
5.8	243	232	306	310
6	271	286	377	373
6.2	269	258	418	389
6.4	251	229	441	452
6.6	212	197	437	391
6.8	154	149	417	437
7	105	114	413	380
7.2	79.8	61.4	328	327
7.4	46.3	32.9	285	274
7.6	31.8	19.4	209	212
7.8	17.7	10.3	142	146

Table 9.1: Effective area as a function of the energy and zenith angle of the simulation.

Effective Area in cm^2

Energy $\log_{10} (E/\text{GeV})$	All angle	
	ν_μ [10^3cm^2]	$\bar{\nu}_\mu$ [10^3cm^2]
3.6	0.164	0.0572
3.8	0.381	0.343
4	1.24	1.07
4.2	3.33	3.15
4.4	8.9	7.51
4.6	17.9	16.7
4.8	31.8	32.6
5	55.6	52.7
5.2	78.9	75.8
5.4	102	103
5.6	136	127
5.8	144	145
6	161	162
6.2	164	155
6.4	157	155
6.6	139	130
6.8	121	126
7	112	102
7.2	86	83.4
7.4	67.8	63.6
7.6	51.2	49
7.8	35.5	34.6

Table 9.2: The angle-averaged neutrino effective area as a function of energy.

Chapter 10

Systematic Uncertainty

A discovery is made if an excess of events over the predicted background is observed in the data. However, due to uncertainties in the simulation, the number of signal and background events predicted may not accurately reflect the true signal and background. Theoretical uncertainties exist in the atmospheric neutrino flux models for several reasons. The cosmic ray spectrum is very uncertain at high energy and hadronic interactions for this energy range are not well understood. There are also detector-related uncertainties. Photons scatter more in dirty or bubble-laden ice. Hence, our incomplete understanding of the dust layers in the ice and the bubbles in the hole ice (formed from water that refroze after deployment of the OMs) add uncertainty to our models [40]. There are also uncertainties in the simulation associated with the modeling of light propagation in the ice and with the optical module sensitivity. These contributions are considered individually to see how they affect the number of simulated events in the final sample. The number of experimental data events remaining after the final energy requirement ($N_{\text{ch}} \geq 100$) is then compared to the range of predicted background and signal events when uncertainties are considered.

10.1 Theoretical Uncertainties in the Background

For this analysis, two models based on the work of Barr *et al.* [50, 52, 53] and Honda *et al.* [51] were considered equally likely options for the conventional atmospheric neutrino simulation. These two models are recent calculations that cover the highest and lowest portion of the atmospheric neutrino flux band created by uncertainties in the primary cosmic ray flux and the high energy hadronic interaction models. Since these models do not extend to the high energies needed for this analysis, the models were extrapolated to higher energies.

10.1.1 Conventional Atmospheric Neutrino Flux based on the Barr *et al.* Model

For this analysis, the Barr *et al.* flux below 10 GeV was taken from [50]. From 10 GeV to 10 TeV, the flux tables from [52], based on the primary spectrum of [53], were used. Above 10 TeV, the weight was derived by performing a 2-dimensional fit with a fifth degree polynomial to the $\log_{10}E$ vs. $\cos(\text{zenith})$ tables of the atmospheric neutrino flux values from lower energies just mentioned. The TARGET version 2.1 [57] hadronic interaction model was used [50].

10.1.2 Conventional Atmospheric Neutrino Flux based on the Honda *et al.* Model

In an attempt to better fit the AMS [58] and BESS [59, 60] data, Honda *et al.* changed the power law fit to the proton cosmic ray spectrum from -2.74 to -2.71 above 100 GeV [51]. Other parameters in the cosmic ray fit remained similar to the Barr *et al.* flux mentioned above [61], although the DPMJET-III [62] interaction model was

used. The atmospheric neutrino weights from [51] were used up to 10 TeV. Above that energy, a 2-dimensional fit of the lower energy values was again used as described above. The result was a lower atmospheric neutrino flux prediction than the Barr *et al.* flux.

10.1.3 Prompt Atmospheric Neutrinos

Conventional atmospheric neutrinos from the decay of pions and kaons are not the only source of atmospheric background. Above 50 TeV - 1 PeV, the source of atmospheric neutrinos is expected to change [33, 35, 36, 34, 30]. Semileptonic decays of short-lived charmed particles become the main contributor to the atmospheric neutrino flux.

10.1.4 Additional Neutrino Flux Uncertainty

Uncertainties were included for both conventional atmospheric neutrino models. The uncertainty in the cosmic ray spectrum was estimated as a function of energy based on the spread of values measured by many cosmic ray experiments [63]. These uncertainties were added in quadrature with the estimated uncertainty due to choosing different hadronic interaction models [50, 51, 61]. Uncertainties were also estimated based on the spread of predictions surrounding the unknown prompt neutrino flux. Unless mentioned otherwise, when prompt neutrinos were included in this work, the average of the Martin GBW (Golec-Biernat and Wüsthoff) [34] and Naumov RQPM (Recombination Quark Parton Model) [35, 36] models is shown. This is henceforth called the central prompt neutrino model.

All of the uncertainty factors for the total (conventional + prompt) atmospheric

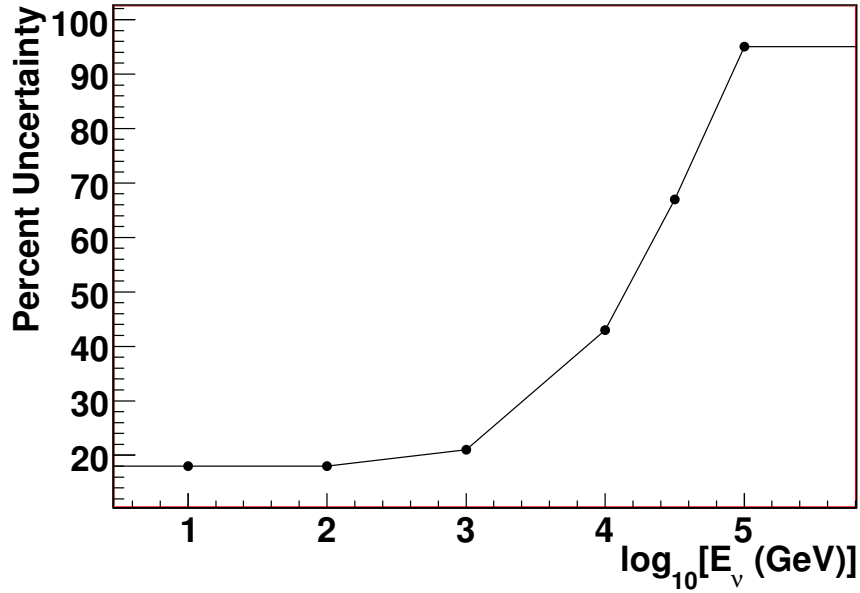


Figure 10.1: The estimated uncertainty in the atmospheric neutrino flux as a function of energy. Due to the large uncertainty in the prompt neutrino flux at greater than 10^4 GeV, the total uncertainty rises sharply.

neutrino flux were combined and are shown as a function of energy in Figure 10.1. Since the true energy of every simulated event is known, each event was given a weight based on the maximum uncertainty estimated for that neutrino energy. As a result, three predictions for the number of atmospheric neutrinos in the final high energy sample were made (the model, the model plus maximum energy-dependent uncertainty, the model minus maximum energy-dependent uncertainty). Since both the Barr *et al.* and Honda *et al.* fluxes were considered equally likely, the central prompt neutrino flux was added to both predictions. Then uncertainties were added and subtracted to both of these total atmospheric neutrino fluxes, creating six different background possibilities.

10.2 Normalizing the Simulation to the Data

After all but the N_{ch} event selection requirements were fulfilled, the N_{ch} distribution for the observed low energy events was inconsistent with that for the total atmospheric neutrino simulation in normalization. Each of the six atmospheric neutrino background predictions was renormalized to match the number of data events observed in the low N_{ch} region, where the signal was insignificant compared to the background. By rescaling the simulation to the number of observed data events, the uncertainty in the atmospheric neutrino flux was reduced to the uncertainty in the spectral shape.

The number of low energy conventional atmospheric neutrinos (second column of Table 10.1) is added to the 4.0 prompt neutrinos predicted with the central prompt neutrino model. The total atmospheric background prediction before renormalization is shown in the third column of Table 10.1. Instead of renormalizing the simulation based on all events with $N_{\text{ch}} < 100$, the renormalization was only based on the region $50 < N_{\text{ch}} < 100$. Because of the difficulty of simulating events near the threshold of the detector, the atmospheric neutrino simulation did not faithfully reproduce the shape of the N_{ch} distribution for the data at N_{ch} below 50. Atmospheric neutrino models were scaled to match the 146 events seen in the experimental data for $50 < N_{\text{ch}} < 100$. The total number of high energy events predicted to survive the final energy requirement is shown before renormalization in the sixth column and after renormalization in the last column.

Since some of the atmospheric neutrino models predicted more events than the data while others predicted less, renormalization of the models to the data brought the

Atms. ν Model	Conv. Atms. ν $50 < N_{\text{ch}} < 100$	Conv. ν + prompt ν $50 < N_{\text{ch}} < 100$	Scale Factor to 146 Low Energy Data Events	Conv. Atms. ν $N_{\text{ch}} \geq 100$	Conv. ν + prompt ν $N_{\text{ch}} \geq 100$	Background Predicted in $N_{\text{ch}} \geq 100$ Sample after Scaling
Barr <i>et al.</i> Max	249.4	253.4	0.58	13.3	14.5	8.3
Barr <i>et al.</i>	193.5	197.5	0.74	9.1	10.3	7.6
Barr <i>et al.</i> Min	137.6	141.6	1.03	4.9	6.1	6.3
Honda <i>et al.</i> Max	191.0	195.0	0.75	9.3	10.5	7.9
Honda <i>et al.</i>	148.7	152.7	0.96	6.4	7.6	7.3
Honda <i>et al.</i> Min	106.5	110.5	1.32	3.4	4.6	6.1

Table 10.1: Number of atmospheric neutrino events predicted by the simulation. Uncertainty in the high energy cosmic ray flux was incorporated into the maximum and minimum predictions.

simulated models into closer agreement. Because this renormalization aimed to correct for theoretical uncertainties in the atmospheric neutrino background prediction, it was not applied to the simulated neutrino signal.

10.3 Simulation Uncertainties

To assure that the detector response to high energy events ($N_{\text{ch}} \geq 100$) is understood, it is important to study high energy events while simultaneously keeping the high energy upgoing events blind to the analyzer. To this end, an inverted analysis was performed in which high quality downgoing tracks were selected from the initial data set. The advantage of studying high quality downgoing tracks is that large data sets are available to study both the high and low energy events. When the data and simulation observable distributions are not perfectly matched, imposing event quality requirements may result in removing different fractions of the simulation in comparison with the data. The inverted analysis was used to study this systematic effect.

10.3.1 Inverted Analysis

For the inverted analysis, all event quality requirements described previously (Table 7.1) were applied, but events were selected based on a high probability of being downgoing rather than upgoing tracks.

When compared to the downgoing experimental data, small shifts were observed in the peaks of the simulated distributions for the number of direct hits (N_{dir}), the smooth distribution of hits along the track (S), the event-by-event track resolution (MR) and likelihood of being downgoing muon tracks rather than upgoing (Inverted Likelihood Ratio, $ILLR$). These discrepancies are most likely due to inaccurate modeling of optical ice properties in the simulation, since it is technically challenging to implement a detailed description of photon propagation through layered ice.

If multiple parameters are correlated, it is possible that mismatches in one parameter may affect the agreement between data and simulation in another. In order to study these effects, the differences in the data and simulation were analyzed at the level where no quality criteria had been applied. The simulated distributions needed to be shifted to larger values by approximately 10% for N_{dir} , 8% for S , 5% for MR and 1% for $ILLR$. When simultaneous corrections to the simulation for all of these effects were applied, the downgoing data and simulation were in better agreement for all parameter distributions. Later in the analysis, these shifts were applied to the upgoing analysis. The number of background and signal events appearing in the final upgoing sample was recalculated based on these simulation shifts.

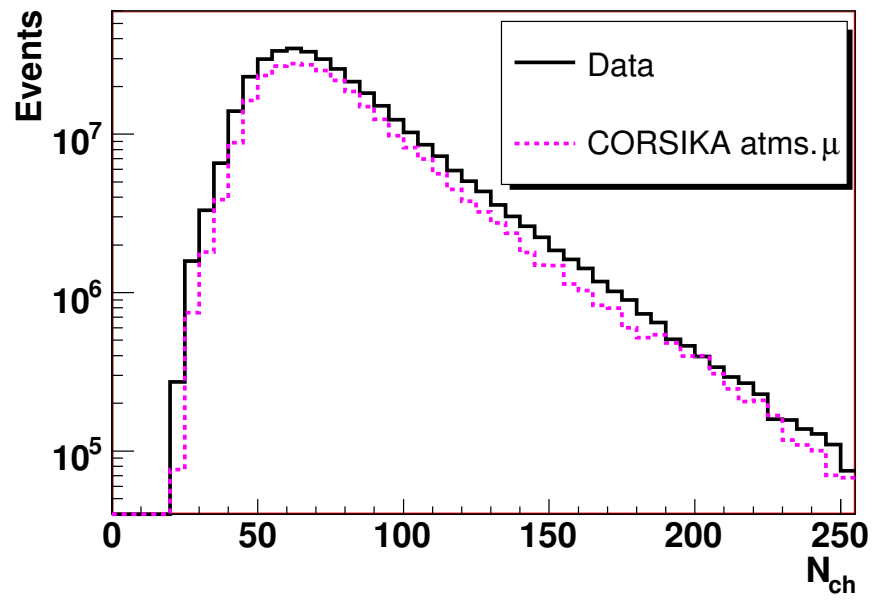


Figure 10.2: In the inverted analysis, the highest quality downgoing events were studied. The N_{ch} distribution is shown for all events which survive the inverted quality requirements.

10.3.2 Uncertainty in Detector Response

The downgoing sample from the inverted analysis was also used to study how well the detector response was simulated in the high energy ($N_{\text{ch}} \geq 100$) regime. Using downgoing data and atmospheric muon simulation, a ratio of the number of events was taken as a function of N_{ch} from the histograms shown in Figure 10.2. If the simulation perfectly described the data, the shapes of the N_{ch} distributions would match and this ratio would be flat. The downgoing ratio was mostly flat, but slightly increased at large N_{ch} where low statistics introduced large uncertainties. The statistical uncertainty aside, a scenario was considered in which the downgoing data to simulation ratio truly increased as N_{ch} increased. Under this scenario, the simulation is renormalized by a larger factor at high N_{ch} to replicate the data. This N_{ch} -dependent renormalization was then applied to the upgoing simulation used for the main part of the analysis. This non-linear normalization factor had a negligible effect in the number of atmospheric neutrinos predicted in the final sample of events with $N_{\text{ch}} \geq 100$. However, the high energy signal simulation event rate increased by 25% when this non-linear N_{ch} effect was included. This uncertainty was incorporated in the final limit calculation that will be described in the next section.

Detection efficiency also depends on the OM sensitivity. This parameter of the simulation was modified and new simulated events were generated. After comparing the data and simulation with different OM sensitivities, a 10% uncertainty in the total number of events due to inaccurate modelling of the OM detection sensitivity was incorporated into the final upper limit calculation.

The systematic errors due to the neutrino interaction cross-section, rock density

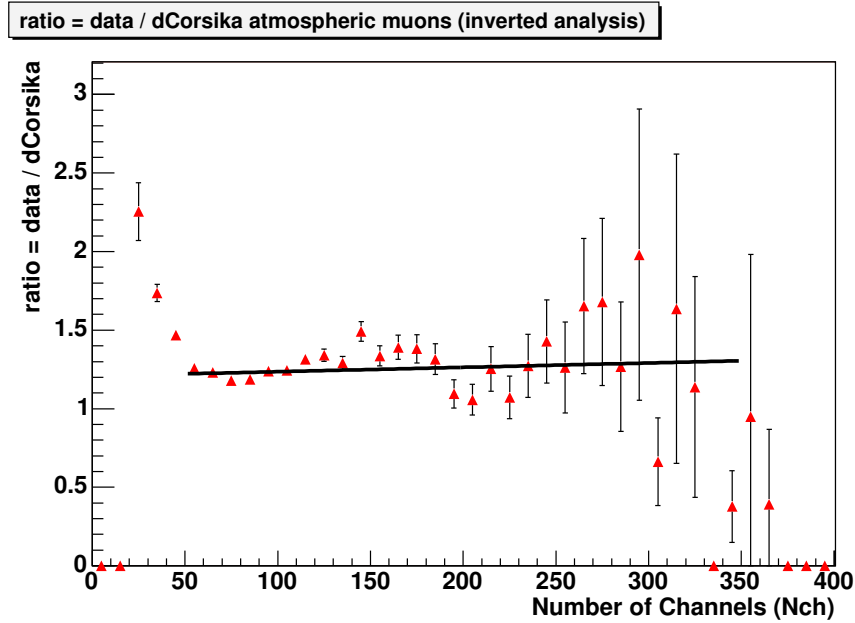


Figure 10.3: Ratio of the number of data events to the number of simulated events as a function of N_c from the inverted analysis.

(below the detector), and muon energy loss do not contribute significantly to this analysis [64].

10.3.3 Relationship between Up and Downgoing Events

In addition to using the inverted analysis to study high energy events and the bias introduced by inaccurate simulation, the downgoing events can be used as a calibration beam for the upgoing atmospheric neutrino flux. To do this, the same model (CORSIKA) was used to describe the downgoing atmospheric muons and the upgoing atmospheric neutrinos [65].

As shown in Table 10.2, the ratio of experimental data to CORSIKA downgoing muon simulation was relatively constant as the event selection became more discriminating. The simulation does not match the data normalization and this may be a

consequence of the theoretical errors in the CORSIKA simulation (mainly due to the hadronic interaction model (QGSJET01) and uncertainty in the primary spectrum ($\Phi \propto E^{-2.7}$)). Another contributing factor to the normalization difference may be that light propagation in the layered ice is modeled inaccurately. When the upgoing CORSIKA atmospheric neutrinos are rescaled based on the downgoing muons, then the upgoing experimental data and CORSIKA atmospheric neutrino simulation are in good agreement for the number of low energy events in the final sample. This can only be seen when the tightest criteria are applied because misreconstructed muons and coincident muons contaminate the data sample when the quality requirements are loose. For instance, at level 5 in the inverted analysis, the ratio of downgoing data to simulation was 1.22. For the upgoing analysis at level 5, 146 events were observed and 124.9 CORSIKA atmospheric neutrinos were predicted. When adjusted based on the inverted analysis, 152.4 ($= 124.9 \times 1.22$) CORSIKA atmospheric neutrinos were predicted, which is in good agreement with the observed value. This shows that it is possible to adjust the normalization of the upgoing events based on the downgoing observations (when the up and downgoing simulation use the same input assumptions about the spectrum and interaction model).

	L1	L2	L3	L4	L5*
<i>Downgoing</i>					
data ($\times 10^8$)	7.88	6.70	6.05	5.89	2.59
CORSIKA atms. μ ($\times 10^8$)	6.63	5.75	5.12	5.01	2.12
ratio	1.19	1.17	1.18	1.18	1.22
<i>Upgoing</i>					
signal	325.4	241.0	190.8	184.8	103.2
coinc μ	2572.8	267.6	45.8	29.4	0
misreconstructed CORSIKA atms. μ	37801.7	2574.8	147.7	34.2	0
Barr <i>et al.</i> atms. ν	680.6	525.9	392.9	379.9	193.5
Honda <i>et al.</i> atms. ν	513.2	399.6	299.9	290.0	148.7
Martin GBW prompt ν	1.9	1.9	1.6	1.5	0.7
Naumov RQPM prompt ν	18.9	18.9	16.0	15.5	7.5
CORSIKA atms. ν	439.9	335.2	251.0	242.5	124.9
Adjusted CORSIKA atms. ν	523.5	392.2	296.2	286.2	152.4
data	276894	24422	1269	531	146

*L5 = level of final analysis

Table 10.2: The number of low energy events ($50 < N_{\text{ch}} < 100$) at a given level for the different types of simulation and experimental data. The top portion of the table presents results from the inverted analysis. The main upgoing analysis is summarized in the lower portion of the table. Note that the upgoing data and adjusted CORSIKA atmospheric neutrino flux are in good agreement when the CORSIKA neutrino events are adjusted by the scale factor determined in the downgoing analysis. This agreement can be seen at the tightest quality levels because all misreconstructed backgrounds have been removed.

Chapter 11

Results

We calculated a confidence interval based on the number of events in the final $N_{\text{ch}} \geq 100$ sample of the predicted background and signal and the observed data. Statistical and systematic uncertainties were incorporated into the confidence interval such that the true, but unknown, value of the diffuse flux of astrophysical neutrinos is contained within the interval in 90% of repeated experiments. A hybrid frequentist-Bayesian method based on the work of Cousins and Highland [66] was used to construct a confidence belt with systematic uncertainties. The likelihood ratio ordering was based on the unified confidence intervals explained by Feldman and Cousins [55]. The uncertainty in the detection efficiency of the signal was set at 27% (10% for optical module sensitivity added in quadrature with 25% for non-linearity in the N_{ch} spectrum when data and simulation are compared). Systematic uncertainties on the number of background events in the final sample were also included in the confidence belt construction. Inclusion of the signal and background uncertainties followed the methods described by Conrad *et al.* [67] and Hill [68].

In constructing the flat Bayesian prior for the background, twelve atmospheric neutrino models were considered equally likely. The twelve predictions were derived

as follows. Initially, two background predictions were considered, Barr *et al.* and Honda *et al.*, each with the central prompt neutrino flux added. To include systematic uncertainties in the models, maximum uncertainties were added and subtracted from each model. Hence, the six predictions were named Barr *et al.* maximum, nominal and minimum and Honda *et al.* maximum, nominal and minimum. The number of events predicted for the background in the final sample is listed in Table 10.1. To account for systematic uncertainties in the detector response, the simulation was shifted in four different parameters. This simulation shift was performed on each of the 6 models described above, hence creating a total of 12 different atmospheric neutrino predictions that were used in the confidence belt construction. The number of events predicted by the 6 models with shifted simulation was within 10% of each number reported in Table 10.1.

11.1 Results for $\Phi \propto E^{-2}$

The signal hypothesis consisted of a flux $E^2\Phi = 1.0 \times 10^{-6} \text{ GeV cm}^{-2} \text{ s}^{-1} \text{ sr}^{-1}$. At this signal strength, 66.7 signal events were expected in the final $N_{\text{ch}} \geq 100$ data. (This value assumes half of the correction from the simulation shifts since 68.4 events were predicted in the final selection, but the number of events decreased to 65.0 when the simulation shifts were applied.) The sensitivity was obtained from the slice of the confidence belt corresponding to zero signal strength. The median observation assuming no signal was seven events, giving a median event upper limit of 6.36 and hence a sensitivity of $9.5 \times 10^{-8} \text{ GeV cm}^{-2} \text{ s}^{-1} \text{ sr}^{-1}$.

When the data with $N_{\text{ch}} \geq 100$ was revealed, six data events were observed. This was consistent with the average expected atmospheric neutrino background of

Event	1	2	3	4	5	6	<i>required value</i>
Year	2001	2001	2001	2001	2002	2003	
Day of Year	118	186	210	274	226	182	
N_{ch}	102	106	157	116	100	111	≥ 100
Track Length [m]	206.7	221.8	197.7	178.2	180.4	207.6	> 170
Number of Direct Hits	27	32	30	22	29	29	> 13
Zenith Angle [$^{\circ}$]	107.3	121.6	106.1	101.8	123.8	113.3	> 100
Median Resolution [$^{\circ}$]	2.4	1.4	1.8	3.0	1.6	2.8	< 4.0

Table 11.1: Observable and reconstructed qualities are shown for the final six events. In addition, events fulfilled requirements based on the reconstructed values of their smoothness (S) and their upgoing vs. downgoing likelihood ratios.

7.0 events (after averaging all models that have been rescaled to the low energy data). Information about the observable quantities for the final six events can be seen in Table 11.1. The final N_{ch} distribution is shown in Figure 8.1. The total number of events predicted for the signal and background can be compared to the observed data in Table 10.2 ($50 N_{\text{ch}} < 100$) and in Table 11.3 ($N_{\text{ch}} \geq 100$). With uncertainties included, the upper limit on a diffuse $\Phi \propto E^{-2}$ flux of muon neutrinos at Earth (90% confidence level) with the AMANDA-II detector for 2000 – 2003 is $7.4 \times 10^{-8} \text{ GeV cm}^{-2} \text{ s}^{-1} \text{ sr}^{-1}$ for 16 TeV to 2.5 PeV. The results are compared to other neutrino limits in Figure 11.1.

11.2 Results for Other Energy Spectra

Other signal models were also tested with this data set. Due to their different energy spectra, the N_{ch} requirement was reoptimized by minimizing the MRF with

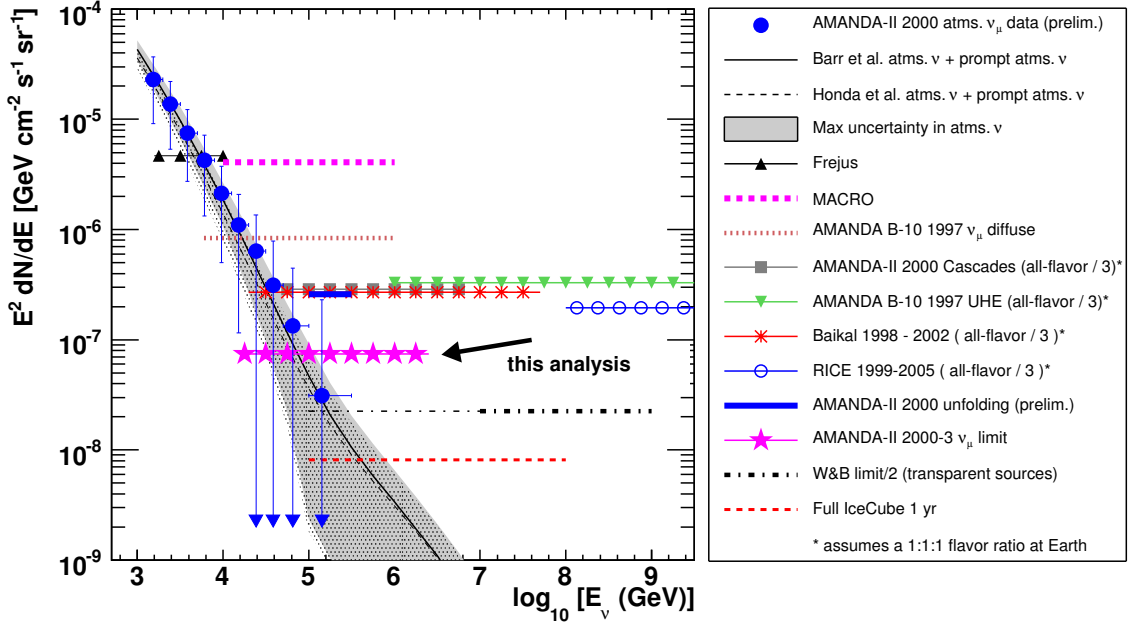


Figure 11.1: The upper limits on the ν_μ flux from sources with an E^{-2} energy spectrum are shown for single and all-flavor analyses. All-flavor upper limits have been divided by three, assuming that the neutrino flavor ratio is 1:1:1 at Earth. The Fréjus [26], MACRO [27], and AMANDA-B10 [24] upper limits on the ν_μ flux are shown, as well as the unfolded atmospheric spectrum from 2000 AMANDA-II data [69]. The AMANDA-II all-flavor limit from 2000 [25], the AMANDA-B10 UHE limit [29], the Baikal five year limit [28] and the RICE six year limit [70] have all been adjusted for the single flavor plot. The $\Phi \propto E^{-2}$ limit from this analysis is a factor of four above the Waxman-Bahcall upper bound. Although not shown, this analysis excludes the $\Phi \propto E^{-2}$ predictions made by Nellen, Mannheim, and Biermann [18] and Becker, Biermann, and Rhode [19] and constrains the MPR upper bound for optically thick pion photoproduction sources [20]. The IceCube sensitivity for a full detector was estimated with AMANDA software [71].

each signal model. For signal models with softer spectra than $\Phi \propto E^{-2}$, a lower N_{ch} requirement was optimal. Five of these models were optimized with a cut on or near 71, so only one unblinding was used for all of these models, $N_{\text{ch}} \geq 71$. Four prompt neutrino models [33, 35, 36, 34] and one astrophysical neutrino model [23] were tested under these conditions. One astrophysical model was optimized at $N_{\text{ch}} \geq 86$ [20]. Two astrophysical neutrino models with harder spectra than $\Phi \propto E^{-2}$ were tested with a higher energy requirement, $N_{\text{ch}} \geq 139$ [20, 21, 22].

Results of these searches are summarized in Table 11.2. The normalization of the overall number of low energy atmospheric neutrinos to data was performed over the region $50 < N_{\text{ch}} < 100$ for the harder spectra ($N_{\text{ch}} \geq 139$), and over $50 < N_{\text{ch}} < 71$ and $50 < N_{\text{ch}} < 86$ for the softer spectra.

When the data from the $N_{\text{ch}} \geq 139$ region were examined, there was good agreement with the expected atmospheric neutrino background (1 event observed on a background of 1.55). For $N_{\text{ch}} \geq 86$, 14 events were observed while an average of 12.9 background events were predicted. However, 37 events were observed while only 27.4 events were expected for $N_{\text{ch}} \geq 71$, leading to a two-sided confidence interval. Since the chance probability of observing 37 or more events on this background is 4%, we do not exclude the background-only null hypothesis. The 90% confidence interval for μ is shown for each model in Table 11.2 and upper limits are calculated based on the upper bound of each confidence interval. If the MRF is greater than 1, then the model is not ruled out based on observations from this four-year data set. Since more events were observed in the data than were predicted by the background simulation for $N_{\text{ch}} \geq 71$, the upper limit on those five models is roughly a factor of three worse

than the sensitivity.

11.2.1 Astrophysical Neutrino Upper Limits

The first astrophysical neutrino model tested with the $N_{\text{ch}} \geq 139$ requirement was initially proposed by Stecker, Done, Salamon and Sommers [21]. The flux tested in this analysis includes the revisions by Stecker, Done, Salamon and Sommers in 1992 [21] and the factor of 20 reduction by Stecker in 2005 [22]. It predicts a flux (Φ_{SDSS}) of high energy neutrinos from the cores of AGNs, especially Seyfert galaxies. Based on the present data, the upper limit on this flux is $1.6 \cdot \Phi_{\text{SDSS}}$. The best previous limit on this model was established by the Baikal experiment, with an upper limit of $2.5 \cdot \Phi_{\text{SDSS}}$ [28].

Mannheim, Protheroe and Rachen (MPR) [20] computed an upper bound for neutrinos from generic optically thin pion photoproduction sources ($\tau_{n\gamma} < 1$), as well as an upper bound for neutrinos from AGN jets. (In addition, they calculated an upper bound for generic optically thick ($\tau_{n\gamma} \gg 1$) pion photoproduction sources assuming a $\Phi \propto E^{-2}$ spectrum, but this is constrained by the results discussed in the previous section.) The upper bounds do not necessarily represent physical neutrino energy spectra, but were constructed by taking the envelope of the ensemble of predictions for smaller energy ranges. Each flux prediction within the ensemble was normalized to the observed cosmic ray proton spectrum.

Nonetheless, the *shapes* of these two upper bounds were tested as if they were models. However, one should be careful not to misinterpret the results. A limit on a model implies a change in the normalization of the entire model. A limit on an upper bound only implies a change in normalization of the bound in the energy region where

the detector energy response to that spectral shape peaks.

The MPR AGN jet upper bound was tested with the $N_{\text{ch}} \geq 139$ requirement. The upper limit on this spectrum is $2.0 \cdot \Phi_{\text{MPRAGN}}$. In comparison, the Baikal upper limit on this spectrum is $4.0 \cdot \Phi_{\text{MPRAGN}}$.

The MPR upper bound for optically thin sources was tested with a $N_{\text{ch}} \geq 86$ requirement. The limit on this spectrum and normalization is $0.22 \cdot \Phi_{\text{MPR}\tau < 1}$.

The remaining neutrino searches were conducted with the lower N_{ch} requirement, $N_{\text{ch}} \geq 71$. A signal hypothesis involving neutrinos from starburst galaxies [23] was tested. Loeb and Waxman assumed that protons in starburst galaxies with energy less than 3 PeV convert almost all of their energy into pions. Their work predicts a range that should encompass the true neutrino spectrum, but the model tested here uses the most probable spectrum from the paper, $\Phi \propto E^{-2.15}$. This analysis assumed the flux was valid for energies ranging from 10^3 to 10^7 GeV. The upper limit on this spectral shape and normalization is $21.1 \cdot \Phi_{\text{starburst}}$.

These astrophysical neutrino models and their observed upper limits based on this data set are shown in Figure 11.2. Neutrino oscillations are taken into account for all models where this factor was not already applied.

11.2.2 Prompt Atmospheric Neutrino Upper Limits

Since prompt neutrinos have a harder (less steep) spectrum than the conventional atmospheric neutrinos, it is possible to search for a prompt neutrino flux by separating the two event classes in energy. The final N_{ch} requirement was reoptimized and the normalization factor was determined based on the interval ($50 \leq N_{\text{ch}} < 71$).

In the astrophysical neutrino searches described thus far, the range of atmo-

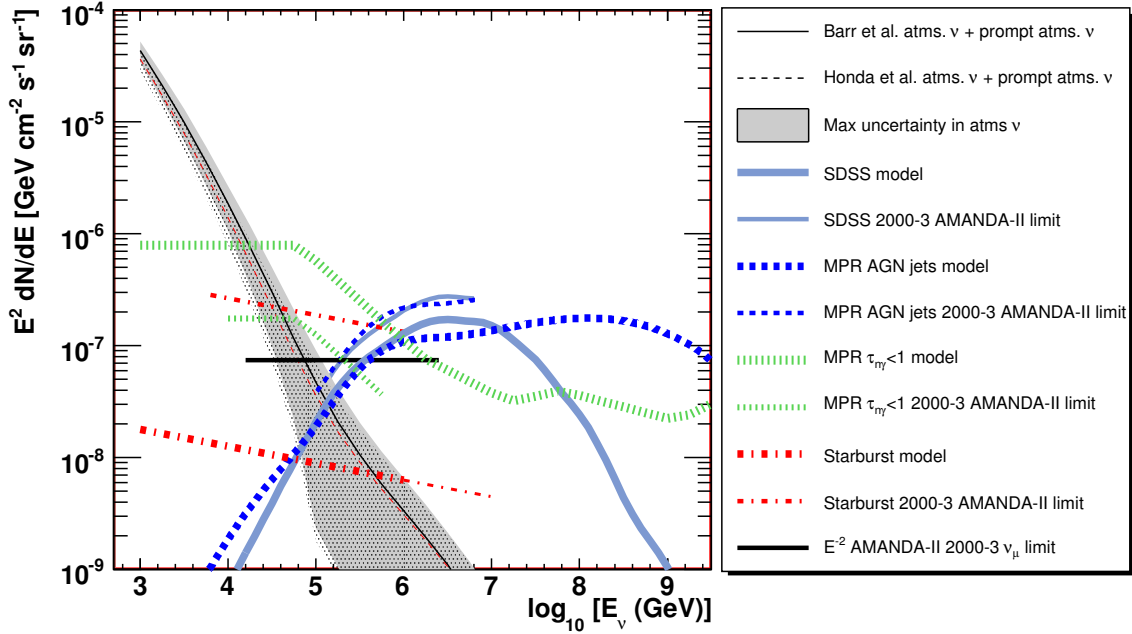


Figure 11.2: Astrophysical neutrino models and upper limits established with this analysis. The Barr *et al.* and Honda *et al.* atmospheric neutrino models are shown as thin lines with maximum uncertainties assumed by this analysis represented by the band. Other models that were tested included the SDSS AGN core model [21, 22], the MPR upper bounds for AGN jets and optically thin sources [20], and a starburst galaxy model [23].

spheric neutrinos predicted in the final sample included an uncertainty due to the unknown prompt neutrino flux. For the search for prompt neutrinos, this uncertainty in the total atmospheric neutrino flux was changed so that only conventional atmospheric neutrino uncertainties were included. Since the atmospheric neutrino simulation was still normalized to the low energy data, the overall effect in the atmospheric background prediction for the final sample was small.

Martin *et al.* predict prompt lepton fluxes based on the GBW model for deep inelastic scattering. This model includes gluon saturation effects [34] which lower the predicted charm production cross sections. The predicted flux is lower than the sensitivity of this data set. The upper limit on this model is $60.3 \cdot \Phi_{\text{MartinGBW}}$.

The Naumov RQPM [35, 36] model of prompt atmospheric neutrinos incorporates data from primary cosmic ray and hadronic interaction experiments. This non-perturbative model includes intrinsic charm [30]. The upper limit on this model is $5.2 \cdot \Phi_{\text{NaumovRQPM}}$.

Prompt neutrinos based on the models of Zas, Halzen and Vazquez were also simulated [33]. A parameterization was established to describe the energy dependence of the charm cross section. For the Charm C model, the charm cross section was fitted to experimental data. In the Charm D model, the cross section was parameterized by Volkova [39]. The upper limit for Charm C is $1.5 \cdot \Phi_{\text{CharmC}}$. However, due to the upward fluctuation in the number of events in the $N_{\text{ch}} > 71$ region, the upper limit on the Charm D model is $0.95 \cdot \Phi_{\text{CharmD}}$. Since the MRF is less than 1.0, the model is disfavored at the 90% confidence level. The prompt neutrino models are shown in Figure 11.3, along with the upper limits based on these data.

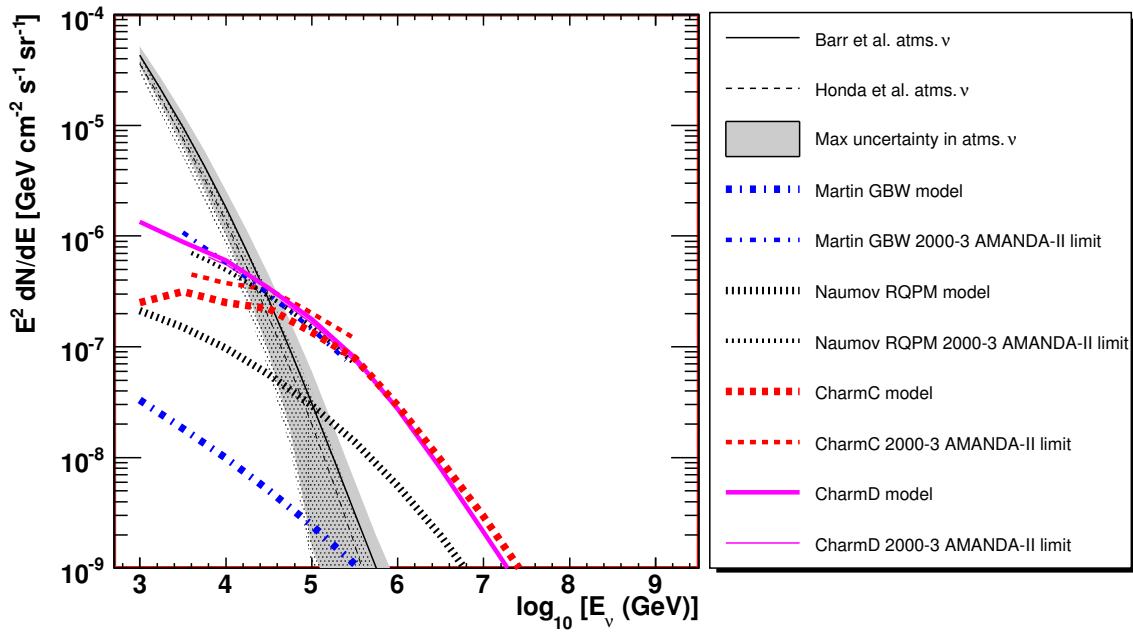


Figure 11.3: Prompt neutrino models and upper limits based on this analysis. The Barr *et al.* and Honda *et al.* atmospheric neutrino predictions are shown for reference. Two charm models [33] were tested, along with the Naumov RQPM [35, 36] and Martin GBW [34] models.

Astrophysical ν

	$\Phi \propto E^{-2}$	SDSS [21, 22]	MPR AGN jets [20]
N_{ch}	100	139	139
n_{b}	7.0	1.55	1.55
n_{s}	66.7	1.74	1.42
$\mu_{\text{median}}(n_{\text{b}})$	6.36	2.86	2.86
sensitivity $\mu_{\text{median}}(n_{\text{b}})/n_{\text{s}} \times \Phi$	$0.095 \times \Phi_{E^{-2}}$	$1.6 \times \Phi_{\text{SDSS}}$	$2.0 \times \Phi_{\text{MPRAGN}}$
n_{obs}	6	1	1
$\mu_{90\% \text{C.I.}}$	(0,4.95)	(0,2.86)	(0,2.86)
upper limit $\mu/n_{\text{s}} \times \Phi$	$0.074 \times \Phi_{E^{-2}}$	$1.6 \times \Phi_{\text{SDSS}}$	$2.0 \times \Phi_{\text{MPRAGN}}$
$(\log_{10} E_{\text{min}}, \log_{10} E_{\text{max}})$	(4.2,6.4)	(5.1,6.8)	(5.0,6.9)

	MPR $\tau_{n\gamma} < 1$ [20]	Starburst [23]
N_{ch}	86	71
n_{b}	12.9	29.1
n_{s}	42.7	1.05
$\mu_{\text{median}}(n_{\text{b}})$	8.48	8.24
sensitivity $\mu_{\text{median}}(n_{\text{b}})/n_{\text{s}} \times \Phi$	$0.2 \times \Phi_{\text{MPR}\tau < 1}$	$7.8 \times \Phi_{\text{Starburst}}$
n_{obs}	14	37
$\mu_{90\% \text{C.I.}}$	(0,9.49)	(0,22.13)
upper limit $\mu/n_{\text{s}} \times \Phi$	$0.22 \times \Phi_{\text{MPR}\tau < 1}$	$21.1 \times \Phi_{\text{Starburst}}$
$(\log_{10} E_{\text{min}}, \log_{10} E_{\text{max}})$	(4.0,5.8)	(3.8,6.1)

Prompt ν

	Martin GBW [34]	Naumov RQPM [35, 36]	CharmC [33]	CharmD [33]
N_{ch}	71	71	71	71
n_{b}	27.4	27.4	27.4	27.4
n_{s}	0.41	4.74	16.05	26.15
$\mu_{\text{median}}(n_{\text{b}})$	8.75	8.75	8.75	8.75
sensitivity $\mu_{\text{median}}(n_{\text{b}})/n_{\text{s}} \times \Phi$	$21.3 \times \Phi_{\text{MGBW}}$	$1.8 \times \Phi_{\text{NRQPM}}$	$0.55 \times \Phi_{\text{CharmC}}$	$0.33 \times \Phi_{\text{CharmD}}$
n_{obs}	37	37	37	37
$\mu_{90\% \text{C.I.}}$	(1.29,24.72)	(1.29,24.72)	(1.29,24.72)	(1.29,24.72)
upper limit $\mu/n_{\text{s}} \times \Phi$	$60.3 \times \Phi_{\text{MGBW}}$	$5.2 \times \Phi_{\text{NRQPM}}$	$1.5 \times \Phi_{\text{CharmC}}$	$0.95 \times \Phi_{\text{CharmD}}$
$(\log_{10} E_{\text{min}}, \log_{10} E_{\text{max}})$	(3.5,5.5)	(3.6,5.6)	(3.8,5.7)	(3.6,5.6)

Table 11.2: Several flux shapes were tested with this data set. N_{ch} is the minimum number of OMs that had to be hit for an event to appear in the final data set. The predicted number of events for background, n_{b} , and signal, n_{s} , were determined by the simulation. The median event upper limit is $\mu_{\text{median}}(n_{\text{b}})$. The sensitivity is the model flux multiplied by the median event upper limit and divided by the number of signal predicted. The number of events observed in the four year data sample is n_{obs} . The upper limit is calculated from the maximum value of the 90% confidence interval for the event upper limit, μ . The upper limit is the test flux multiplied by μ/n_{s} . All values quoted here incorporate systematic uncertainties.

Upgoing $N_{\text{ch}} \geq 100$						
	L0	L1	L2	L3	L4	L5
signal		160.4	123.7	103.7	103.2	68.4
coinc. μ		54.2	4.3	2.8	2.8	0
misreconstructed CORSIKA atms. μ		862.1	35.4	0	0	0
Barr <i>et al.</i> atms. ν		36.0	27.6	19.3	18.9	9.1
Honda <i>et al.</i> atms. ν		25.2	19.3	13.5	13.2	6.4
Martin GBW prompt atms. ν		0.42	0.42	0.36	0.36	0.19
Naumov RQPM prompt atms. ν		4.8	4.8	4.2	4.2	2.2
Data		11456	1347	96	45	6
Downgoing $N_{\text{ch}} \geq 100$						
CORSIKA atms. $\mu (\times 10^7)$	7.31		6.53	6.05	6.01	5.09
data ($\times 10^7$)	9.75		8.59	8.07	8.03	6.60

L5 = level of final analysis

Table 11.3: The number of high energy events ($N_{\text{ch}} \geq 100$) at a given quality level for the different types of simulation and experimental data.

Chapter 12

Future Techniques for Diffuse Analyses

This analysis relied on a *cut and count* method to set an upper limit on the diffuse flux of astrophysical and prompt neutrinos. Seven background events were predicted to exist in the high energy $N_{\text{ch}} \geq 100$ sample. Six events were observed and the astrophysical neutrino upper limit was established based on the observation of roughly the same number of data events as were predicted by the background simulation. By simply cutting and counting, any excess that might be observed could not be identified certainly as being astrophysical in origin. It could be possible that some or all of the excess actually comes from prompt atmospheric neutrinos. In order to overcome this problem in this analysis, assumptions were made about the prompt neutrino flux in order to set an astrophysical neutrino limit. (And vice versa.)

For the astrophysical neutrino search, it was assumed that the prompt atmospheric neutrino flux was equal to the average of the Naumov RQPM and Martin GBW models. Currently, the range in which the prompt neutrino flux is expected to lie is bounded at the high end by the Naumov RQPM model. The Martin GBW model marks the lower boundary of the predicted flux region.

The uncertainty in the prompt neutrino flux spans orders of magnitude and

assuming a certain background flux due to these types of events could potentially be misleading. Since no excess of events was observed in the astrophysical search, it was then assumed that no astrophysical neutrino flux was present so that an upper limit on the prompt atmospheric flux could be placed. However, it would make more sense to place two-dimensional limits on the astrophysical and prompt atmospheric fluxes at the same time.

Two-dimensional limits show an allowed region in which the astrophysical and prompt atmospheric neutrino fluxes may lie and be consistent with the observed data. By finding an allowed region in two-space, assumptions do not have to be made about either type of flux.

Cut and count methods do not consider shape information about the predicted or observed spectrum of events. The next diffuse analysis will compare the shape and normalization of the observed data to simulations based on different background and signal flux models. N_{ch} and the reconstructed zenith angle of the track were powerful parameters used in this analysis and they will be used to calculate likelihoods of the different models based on the observed data. By using shape and normalization information for N_{ch} and the reconstructed zenith angle, it is hoped that the conventional atmospheric neutrino background can be better understood (for instance, we could determine which conventional atmospheric neutrino model is correct... or most correct).

Multiple two-dimensional limits will need to be published when this method is used (for instance, a two-dimensional limit on the diffuse flux of $\Phi \propto E^{-2}$ neutrinos versus prompt atmospheric neutrinos as predicted by Martin GBW). Another two-

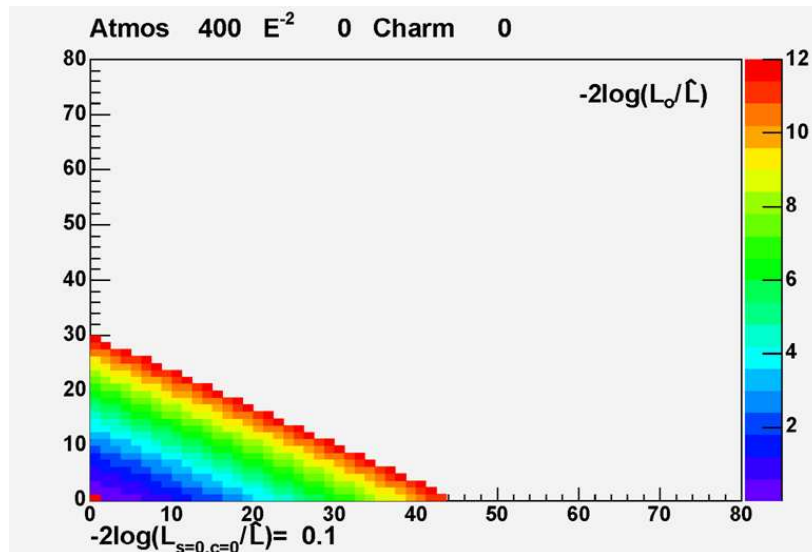


Figure 12.1: Two-dimensional upper limits can be established without making *a priori* assumptions about the amount of astrophysical or prompt atmospheric neutrino flux in the data. The x-axis represents the upper limit on the prompt atmospheric neutrino flux while the y-axis represents the upper limit on astrophysical neutrinos.

dimensional region would have to be published in order to constrain the Naumov RQPM model, for instance.

Chapter 13

Conclusions

The experimental data were consistent with the predicted range of atmospheric neutrino background. Six high energy events were observed in the final data set, while the average predicted background was 7.0 events. There is no indication of an astrophysical signal. At a 90% confidence level, the diffuse flux of extraterrestrial muon neutrinos with an E^{-2} spectrum is not larger than $7.4 \times 10^{-8} \text{ GeV cm}^{-2} \text{ s}^{-1} \text{ sr}^{-1}$ for 16 TeV – 2.5 PeV.

This analysis also provides upper limits on four astrophysical neutrino models and four prompt neutrino models. For the hardest signal spectra, the results are consistent with background. The softer spectra were tested with lower N_{ch} requirements and despite the observation leading to a two-sided 90% confidence interval, the level of excess is not significant enough to claim a detection.

Before requiring events to fulfill $N_{\text{ch}} \geq 100$, the observed events were compared to the atmospheric neutrino simulation with systematic uncertainties included. The observed low energy data were used to normalize the atmospheric neutrino simulation, hence narrowing the range of atmospheric neutrinos predicted by the different models for the final high energy sample. Systematic effects of the event selection procedure

were studied in the inverted analysis using atmospheric muons. A consistency was established between the observed downgoing atmospheric muon flux and the upgoing atmospheric neutrino flux using the inverted analysis.

This result is the best upper limit on the diffuse flux of TeV – PeV muon neutrinos to date. The upper limit is an order of magnitude lower than the previous AMANDA result by performing a multi-year analysis [24] and by using a larger detector, AMANDA-II instead of AMANDA-B10. For a $\Phi \propto E^{-2}$ spectral shape, this analysis provides an upper limit that is a factor of three better than the Baikal muon neutrino upper limit (muon neutrino upper limit = all-flavor limit/3 assuming a 1:1:1 flavor ratio).

This analysis set upper limits on four prompt atmospheric neutrino predictions, while one of these models is disfavored at a 90% confidence level. Other spectral shapes were tested for astrophysical neutrinos. No models were excluded, however constraints were placed on the existing predictions. The shapes of the MPR upper bounds were tested in the energy region where the detector response peaks. For the benchmark $\Phi \propto E^{-2}$ spectral shape, the current limit is a factor of 4 above the Waxman-Bahcall upper bound.

AMANDA-II has now been integrated into IceCube. The sensitivity of the IceCube detector will continue to improve as the detector grows to its final volume, 1 km³. Based on estimations with AMANDA software, the full IceCube detector will have a sensitivity that is a factor of 10 better than this analysis after one year of operation [71].

Bibliography

- [1] M. Longair, *High Energy Astrophysics*, Vol. 1, Cambridge University Press, Cambridge (1992).
- [2] C. Lefevre, *LHC: the guide*, CERN Document Server, <http://cdsweb.cern.ch/collection/Official%20Press%20Brochures>.
- [3] T.K. Gaisser, *Cosmic Rays and Particle Physics*, Cambridge University Press (1990).
- [4] G. Sigl, hep-ph 0109202 (2001).
- [5] J. Learned and K. Mannheim, *Annu. Rev. Nucl. Part. Sci.*, 50 679 (2000).
- [6] M. Takeda *et al.*, *Astrophys. J.* **522**, 225 (1999).
- [7] F. Aharonian *et al.*, *Astrophys. J.* **636**, 777 (2006).
- [8] J. Albert *et al.*, *Astrophys. J.* **648**, L105-L108 (2006).
- [9] H. Athar, M. Jezabek, and O. Yasuda, *Phys. Rev. D* **62**, 103007 (2000).
- [10] T. Kashti and E. Waxman, *Phys. Rev. Lett.* **95**, 181101 (2005).

- [11] M. Longair, *High Energy Astrophysics*, Vol. 2, Cambridge University Press, Cambridge (1994).
- [12] K. Greisen, *Annu. Rev. Nucl. Sci.* **10**, 63 (1960).
- [13] F. Reines, *Annu. Rev. Nucl. Sci.* **10**, 1 (1960).
- [14] M.A. Markov and I.M. Zheleznykh, *Nucl. Phys.* **27**, 385 (1961).
- [15] E. Waxman and J. Bahcall, *Phys. Rev. D* **59**, 023002 (1998).
- [16] J. Bahcall and E. Waxman, *Phys. Rev. D* **64**, 023002 (2001).
- [17] E. Waxman, *Nucl. Phys. Proc. Suppl.* **118**, 353 (2003).
- [18] L. Nellen, K. Mannheim, and P.L. Biermann, *Phys. Rev. D* **47**, 5270 (1993).
- [19] J. Becker, P. Biermann, and W. Rhode, *Astropart. Phys.* **23**, 355 (2005).
- [20] K. Mannheim, R.J. Protheroe, and J.P. Rachen, *Phys. Rev. D* **63**, 023003 (2000).
- [21] F.W. Stecker, C. Done, M.H. Salamon, and P. Sommers, *Phys. Rev. Lett.* **66**, 2697 (1991); **69**, 2738(E) (1992).
- [22] F.W. Stecker, *Phys. Rev. D* **72**, 107301 (2005).
- [23] A. Loeb and E. Waxman, *J. Cosmol. Astropart. Phys.* JCAP05 003 (2006).
- [24] J. Ahrens *et al.*, *Phys. Rev. Lett.* **90**, 251101 (2003).
- [25] M. Ackermann *et al.*, *Astropart. Phys.* **22**, 127 (2004).

- [26] W. Rhode *et al.* (Fréjus Collaboration), *Astropart. Phys.* **4**, 217 (1996).
- [27] M. Ambrosio *et al.* (MACRO Collaboration), *Astropart. Phys.* **19**, 1 (2003).
- [28] V. Aynutdinov *et al.*, *Astropart. Phys.* **25**, 140 (2006).
- [29] M. Ackermann *et al.*, *Astropart. Phys.* **22**, 339 (2005).
- [30] C.G.S. Costa, *Astropart. Phys.* **16**, 193 (2001).
- [31] W.-M. Yao *et al.*, *J. Phys. G* **33**, 1 (2006).
- [32] G. Thunman, G. Ingelman, and P. Gondolo, *Astrop. Phys.* **5**, 309 (1996).
- [33] E. Zas, F. Halzen, and R.A. Vázquez, *Astropart. Phys.* **1**, 297 (1993).
- [34] A.D. Martin, M.G. Ryskin, and A.M. Stasto, *Acta Phys. Polon.* **B34**, 3273 (2003).
- [35] G. Fiorentini, A. Naumov, and F.L. Villante, *Phys. Lett. B* **510**, 173 (2001).
- [36] E.V. Bugaev *et al.*, *Il Nuovo Cimento* **12C**, No. 1, 41 (1989).
- [37] E.V. Bugaev *et al.*, *Phys. Rev. D* **58**, 054001 (1998).
- [38] O. Botner *et al.*, *Phys. Lett. B* **236**, 488 (1990).
- [39] L.V. Volkova *et al.*, *Il Nuovo Cimento* **C10**, 465 (1987).
- [40] M. Ackermann *et al.*, *J. Geophys. Res.* **111**, D13203 (2006).
- [41] D. Heck, J. Knapp, J.N. Capdevielle, G. Schatz, and T. Thouw, *Tech. Rep.* FZKA 6019, Forschungszentrum Karlsruhe (1998).

- [42] J. Ahrens *et al.* (AMANDA Collaboration), Nucl. Instr. Meth. A **524**, 169 (2004).
- [43] M. Ackermann, Searches for signals from cosmic point-like sources of high energy neutrinos in 5 years of AMANDA-II data, Ph.D. thesis, Humboldt-Universität zu Berlin (2006).
- [44] D. Pandel, Diploma Thesis, Humboldt-Universität zu Berlin, Berlin, Germany, February 1996.
- [45] I. Taboada, Search for High Energy Neutrino Induced Cascades with the AMANDA-B10 Detector, Ph.D. thesis, University of Pennsylvania (2002).
- [46] A. Pohl, A Statistical Tool for Finding Non-Particle Events from the AMANDA Neutrino Telescope, Ph.D. thesis, Kalmar University and Uppsala Universitet (2004).
- [47] T. Neunhoffer, Astropart. Phys. **25**, 220 (2006).
- [48] G.C. Hill, Astropart. Phys. **6**, 215 (1997).
- [49] P. Lipari, Astropart. Phys. **1**, 195 (1993).
- [50] G.D. Barr, T.K. Gaisser, P. Lipari, S. Robbins, and T. Stanev, Phys. Rev. D **70**, 023006 (2004).
- [51] M. Honda, T. Kajita, K. Kasahara, and S. Midorikawa, Phys. Rev. D **70**, 043008 (2004).

- [52] G. Barr, T.K. Gaisser, P. Lipari, S. Robbins, and T. Stanev, <http://www-pnp.physics.ox.ac.uk/~barr/fluxfiles/>.
- [53] T.K. Gaisser, M. Honda, P. Lipari, and T. Stanev, in *Proceedings of the 27th International Cosmic Ray Conference*, Hamburg, Germany, **5**, 1643 (2001).
- [54] G.C. Hill and K. Rawlins, *Astropart. Phys.* **19**, 393 (2003).
- [55] G.J. Feldman and R.D. Cousins, *Phys. Rev. D* **57**, 3873 (1998).
- [56] L. Gerhardt for the IceCube Collaboration, in *Proceedings of the 29th International Cosmic Ray Conference*, Pune, India, **5**, 111 (2005), astro-ph 0509330.
- [57] R. Engel *et al.*, in *Proceedings of the 27th International Cosmic Ray Conference*, Hamburg, Germany, 1381 (2001).
- [58] J. Alcaraz *et al.* (AMS Collaboration), *Phys. Lett. B* **490**, 27 (2000).
- [59] T. Sanuki *et al.*, *Astrophys. J.* **545**, 1135 (2000).
- [60] S. Haino *et al.*, *Phys. Lett. B* **594**, 35 (2004).
- [61] T.K. Gaisser, in *Proceedings of Nobel Symposium 129 "Neutrino Physics"*, astro-ph 0502380 (2005).
- [62] S. Roesler, R. Engel, and J. Ranft, in *Proceedings of the 27th International Cosmic Ray Conference*, Hamburg, Germany, **1**, 439 (2001); *Phys. Rev. D* **57**, 2889 (1998).
- [63] T.K. Gaisser and M. Honda, *Annu. Rev. Nucl. Part. Sci.* **52**, 153 (2002).

- [64] A. Achterberg *et al.*, astro-ph 0611063 (2006).
- [65] D. Chirkin, hep-ph 0407078 (2004).
- [66] R.D. Cousins and V.L. Highland, Nucl. Instrum. Methods Phys. Res. A **320**, 331 (1992).
- [67] J. Conrad, O. Botner, A. Hallgren, and C. Pérez de los Heros, Phys. Rev. D **67**, 012002 (2003).
- [68] G.C. Hill, Phys. Rev. D **67**, 118101 (2003).
- [69] K. Münich for the IceCube Collaboration, in *Proceedings of the 29th International Cosmic Ray Conference*, Pune, India, **5**, 17 (2005), astro-ph 0509330.
- [70] I. Kravchenko *et al.*, Phys. Rev. D **73**, 082002 (2006). The value of the upper limit is taken from Figure 19. S. Hussain (private communication).
- [71] J. Ahrens *et al.*, Astropart. Phys. **20**, 507 (2004).

Appendix A

Q&A for the Non-Physicist

What are neutrinos? How do we detect them? Why is the AMANDA detector located at the South Pole? What can we learn by studying neutrinos? These are among the first questions asked by people who want to learn about IceCube and neutrino science. This chapter is intended to explain basic neutrino astrophysics to the *non*-physicist. Each section title is a question I've been asked during my time on this project.

A.1 What are neutrinos?

The basic particles that make up atoms are protons (positive charge), neutrons (no charge) and electrons (negative charge). Protons and neutrons (not neutrinos!) belong to a family called hadrons. Hadrons are formed from even smaller constituents known as quarks and gluons. On the other hand, electrons are members of the lepton family. Leptons cannot be broken down into smaller constituents. Neutrinos are also in the lepton family and are very tiny, chargeless particles.

There are three types of charged leptons and each one has a neutrino partner. Electrons (e), muons (μ) and taus (τ) are all *cousins*. Taus are the heaviest, then muons, then electrons. There is a corresponding neutrino *flavor* for each of the charged

e^+, e^-	electron, positron	$\nu_e, \bar{\nu}_e$	electron neutrino, electron anti-neutrino
μ^+, μ^-	muon	$\nu_\mu, \bar{\nu}_\mu$	muon neutrino, muon anti-neutrino
τ^+, τ^-	tau	$\nu_\tau, \bar{\nu}_\tau$	tau neutrino, tau anti-neutrino

Table A.1: The lepton family.

particles. We call them ν_e , ν_μ and ν_τ . Each neutrino also has an anti-neutrino partner which is denoted by the same symbol with a line or bar placed above it. Neutrinos were originally thought not to have any mass, although it has since been proven that they do. The lepton family is summarized in Table A.1.

Every second about one trillion (1,000,000,000,000) neutrinos travel harmlessly through your body. Because neutrinos are so incredibly small, most of the time they pass right through solid objects without interacting at all. Neutrinos very rarely interact with other atoms and they are constantly bombarding everything around us. They travel at almost the speed of light - that is 300,000,000 meters every second - or 670 million miles per hour.

A.2 Why do we care about neutrinos?

We have much to learn about neutrinos! The neutrino wasn't postulated until 1930 and wasn't discovered until the 1950s. With trillions of neutrinos traveling through you all the time from all directions, the neutrinos must come from many sources. For instance, neutrinos are created during radioactive decays, such as the breakdown of Potassium in the human body. Experiments have detected neutrinos produced by nuclear reactors, as well as those created by particle interactions in the upper atmosphere. Further out in space, neutrinos are formed inside stars, including the Sun.

The Sun has been studied for centuries and we now have a good understanding of the mechanisms that make the Sun burn. As a result, we know how old it is and how long we expect it to burn. Even though we can never travel there, we have found ways to explain the particle interactions occurring there. We now understand, for instance, that the Sun burns because energy is being released every time two protons fuse together. Neutrinos are created in the Sun and other neutrino experiments have detected these neutrinos.

On the other hand, the Earth and Sun are only tiny blips on the cosmic radar. Stars and galaxies abound. They are so far away from us that we will never be able to send a spaceship or probe to study them. However, just as we want to know how the particles in the Sun interact, we would like to know how the particles in other stars and galaxies are interacting. We think that neutrinos are playing active roles in these distant objects, but we won't know for sure until we detect them. Since stars and galaxies are so far away from us, we must study them based on the clues that *they* send to *us*.

There are three main types of telescopes or detectors studying distant space. They each detect a different type of particle.

1. Optical telescopes. These detectors study light from space. The light can arrive anywhere along the electromagnetic spectrum. That means that the light output could be optical (light that we see with our eyes) or it could be in radio waves (long) or ultraviolet or x-rays (short), for instance. Gamma-rays have the shortest wavelengths and carry the most energy.
2. Cosmic ray detectors study charged particles traveling in space. Cosmic rays are

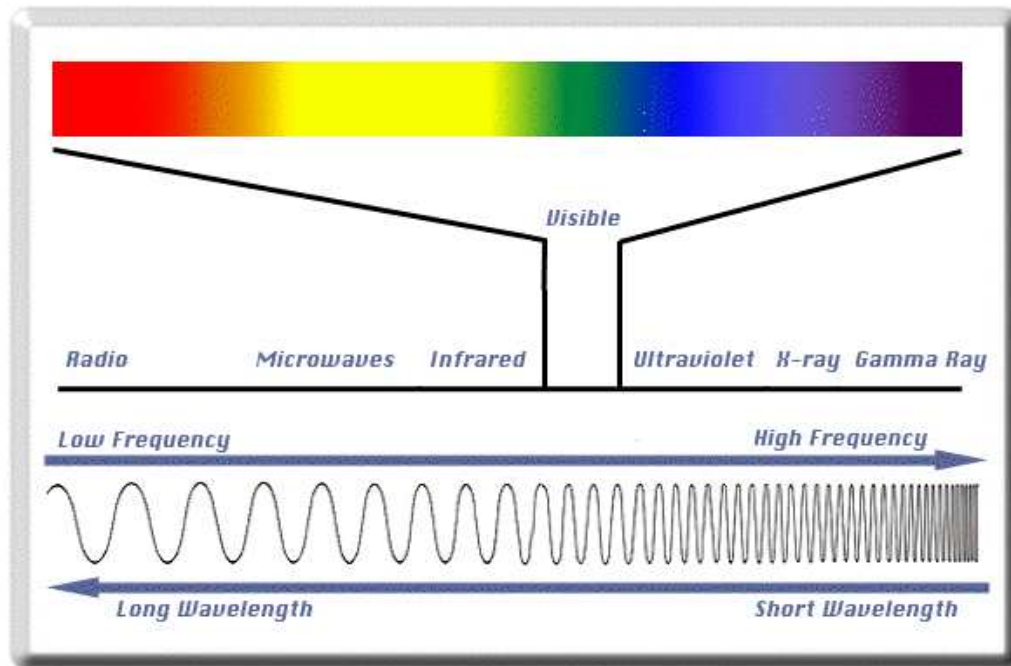


Figure A.1: Electromagnetic spectrum. Image credit: Laboratory for Computational Science and Engineering, University of Minnesota.

mainly protons.

3. Neutrinos telescopes search for neutrinos.

There are advantages and disadvantages to each of these three ways of studying the Universe. The important point, though, is that all of these methods complement each other. We should pursue all of the detection methods in order to gain the best understanding of the Universe. Light is the traditional way in which we have studied the skies. However, sometimes the light is absorbed by other objects in space and does not make it all the way to the Earth. Cosmic rays, on the other hand, are also fairly easy to detect. However, because they have positive or negative charge, the direction that they are traveling can be changed as they travel through magnetic fields in space.

That means that we will never know their direction of origin. Neutrinos, on the other hand, are important messengers because they always travel in straight lines - directly from the source to the point where they are detected. Because neutrinos do not have any charge, magnetic fields in space cannot change their direction. Neutrinos do not interact with matter very often. In fact, they often travel through the Earth (and your body!) without even noticing. Since they rarely interact, large detectors are needed to observe an interaction.

A.3 What objects in space are we studying?

The explosion of a star is called a supernova and we know that these events produce neutrinos. They were documented in coincidence with a supernova that occurred in 1987.

Gamma-ray bursts (GRBs) are yet another type of astronomical object that we are studying. Gamma rays are at the highest end of the electromagnetic spectrum, meaning that these photons of light have the highest energy possible. When there is a quick burst of gamma-rays (light) in the sky (anywhere from about 1 to 100 seconds), it is called a GRB. Hundreds of GRBs have been identified and clues are indicating that they may be closely related to supernovae. We also believe that neutrinos are involved in these events and we would like to understand better how they happen.

An AGN, or active galactic nuclei, is a galaxy that most likely has a black hole at its center. These galaxies have very strong light emission. The light can occur anywhere along the electromagnetic spectrum - in optical, radio waves, ultraviolet (UV) or x-rays for example. The light output from an AGN can occur in streams or jets, where most of the particles travel out of the AGN in one of two directions

(pointing exactly opposite). We do not yet fully understand what particle interactions are fueling this behavior, but it seems likely that neutrinos are involved. If we find neutrinos are originating in AGN, it will be a major step toward understand how AGN and their associated black holes work.

A.4 How we detect neutrinos?

Because neutrinos rarely interact, we need a very large detector to increase our chance of an interaction occurring. Here, I will focus on detecting the muon neutrino, ν_μ , since that flavor was the focus of this analysis. When a muon neutrino hits an atom (remember that they usually pass right between them), an interaction occurs. The neutrino ceases to exist and a muon is formed. The muon then gives off light as it travels in the same direction as the neutrino was going. The AMANDA and IceCube detectors are built to detect the light that is given off as the muon travels. The reason the detectors are located deep in the ice at the South Pole is that a large, clear medium is needed. Otherwise, the light couldn't be detected! Water and ice are ideal for these detectors because they are cheap. Where else would you find a cubic kilometer of a clear medium? Similar detectors are being built or are operating in lakes and the Mediterranean Sea.

A.5 How does the AMANDA detector work?

The AMANDA detector contains 677 light sensors. These light sensors are buried in the ice so that they can detect the light from the muons. The sensors are connected along 19 cables and form a three dimensional array. To install each string in the ice, a hot water drill made a very deep, narrow hole. Once the ice was melted and the

hole contained water, the cable was lowered into the hole. Every 15 meters, a light sensor was attached. The 19 AMANDA strings are located such that each string is at least 25 – 50 meters from any other. When the muon emits light, the light sensors closest to the muon record a signal. This continues as the particle travels through the ice emitting light. The path of the muon is then identified by the sequence in which the light sensors recorded seeing something. Since the neutrino and muon it produces always travel in the same direction, we can reconstruct the direction of the neutrino and point back to the exact direction in space where it originated.

A.6 How does my analysis work?

Some AMANDA analyses perform point source searches of the sky. This means that we look for neutrinos coming from a particular direction in the sky because we know that there is an active galaxy or other object there. However, neutrinos have not yet been found by looking at specific objects.

Consider this scenerio (in which none of the numbers are real). Let's say that if I look in the direction of a specific AGN with the AMANDA detector, I expect 50 events in my background. The background events are always there, although maybe at times there are more or less than 50 (say 46 or 57 background events, for example). In order to say that the AGN is a neutrino source, I must be able to say that there are many more neutrinos than I would expect in my background. If I measured 60 neutrinos, I probably would not be able to say with certainty that the neutrinos came from the AGN. It could have happened that there were 50 background events and 10 signal events. However, it would also be quite possible that the background was just a little bit higher than normal and all 60 events were background. However, if I

measure 100 neutrinos and only expected 50, then it is likely that the AGN is creating the neutrinos that I detected.

Unfortunately, no *point sources* of neutrinos have been identified by searching for neutrinos from a specific direction. Another method can be used to make it easier to detect a neutrino source and the following analysis technique was used in the analysis described in this thesis. Let's say that we search for a signal from all of the AGN across the entire sky. For simplicity, let's assume that there are 20 AGN, although this is obviously a gross underestimate! Across the entire sky, I expect 500 background events. If I observe 700 events, that is 200 more events than I expected in my background. It would then seem very likely that a neutrino source is creating these extra events and they are not background! If there are 20 total AGN and 200 extra events over the expected background, that means that 10 events had to come from each AGN (that is $200/20 = 10$). Note that 10 neutrinos was not enough to claim an AGN neutrino detection in the point source search I described earlier. However, if many sources each contribute 10 events, then together all of the distant AGN are identified as neutrino sources. This method is called a *diffuse* search for neutrinos.

For this analysis, I began with 5,200,000,000 events that triggered the detector between February 2000 and November 2003. I then had to throw away all of the events that were obviously background. In the end, I predicted a background of 7 events. When I looked at the data, I observed 6 events, a slight fluctuation from the predicted value. Since I did not see a large excess of events over the predicted background, I did not claim to observe any neutrino signal from astronomical objects like AGN.

However, we can still learn from the analysis even though we did not observe

neutrinos from other galaxies or objects. We can set an *upper limit* on how strong those sources of neutrinos could actually be. Let's return to the scenario from above. If 500 events were predicted and 520 events were observed, we would not claim to see any astrophysical neutrino signal. It could have been that each of the 20 AGN contributed 1 event in addition to the background of 500, however 520 could just be a background fluctuation. However, we can say that *if the AGN were putting out 10 neutrinos each, then we would have observed 700 events and would have claimed detection of a neutrino signal*. Hence, since that did not happen, we know that each AGN must emit *less than* 10 neutrinos. That is the maximum amount of neutrinos that the source could emit and still be consistent with what we observed. We call this an upper limit. We have learned something - we have learned that AGN put out less than 10 neutrinos each. (Don't forget... all of these numbers are fake!)

The longer the detectors are turned on, the more likely it is we will detect a signal. The IceCube detector will be much larger than the AMANDA detector and this will increase the probability of identifying distant neutrino sources.

A.7 Summing it up, plain and simple

Neutrinos are tiny, chargeless particles. Most of the time, they pass harmlessly through matter because they do not like to interact.

Neutrinos provide valuable information to physicists and astronomers because they travel in straight lines. When a neutrino is detected, we can trace backward to find the direction of origin and possibly the source. We hope to identify objects in space that are producing neutrinos that we can detect here on Earth. These objects might be supernovae (exploding stars), gamma-ray burts (objects that cause very

quick, bright flashes of light) or active galactic nuclei (galaxies with black holes at the center).

The AMANDA detector uses a 3-dimensional array of light sensors to search for the light emitted by particles after a neutrino hits an ice molecule and interacts. Since we are detecting light, we need a large, clear medium. The detector is buried at the South Pole because the ice is very pure and the light can travel long distances in the ice.